U.S. DEPARTMENT OF COMMERCE
National Oceanic and Atmospheric Administration
Environmental Research Laboratories

NOAA Technical Memorandum ERL NSSL-61

GRAVITY CURRENT MODEL APPLIED TO ANALYSIS OF SQUALL-LINE GUST FRONT

Jess Charba

National Severe Storms Laboratory
Norman, Oklahoma
November 1972

TABLE OF CONTENTS

		Page
LIST OF FIGURES		v
LIST OF TABLES		ix
ABSTRACT		x
1.	INTRODUCTION	1
2.	METHODS OF DATA PROCESSING AND ANALYSIS	2
	2.1 Special Data Used	2
	2.2 Data Extracting and Smoothing	3
	2.3 Time-to-Space Conversions	3
	2.4 Special Analysis Techniques	4
	2.5 Concluding Comments on Analysis Approach	6
3.	EVOLUTION OF SQUALL LINE WITHIN LARGE-SCALE WEATHER PATTERN	6
	3.1 Synoptic	6
	3.2 Sub-Synoptic	6
4.	EVOLUTION OF THE SQUALL-LINE THUNDERSTORMS AND GUST FRONT THAT ENTERED THE NETWORK	10
	4.1 Echo Patterns and Related Wind Damage	10
	4.2 Echo Characteristics and Related Wind Damage	14
	4.3 Origin and Evolution of the Gust Front Entering The Network	15
	4.4 Concluding Remarks	15
5.	ANALYTICAL STRUCTURE OF THE THUNDERSTORM OUTFLOW LEADING THE SQUALL LINE	17
	5.1 Displacement Character of Squall System	17
	5.2 Analytical Structure	18
	5.2.1 Windshift	18
	5.2.2 Gust Front	23
6.	APPLICATION OF THEORIES AND MODELS TO THE ANALYSIS	28
	6.1 Relationship of Windshift to Gust Front	28
	6.2 Gravitational Wave Model Applied to Windshift	30
	6.3 Gravity Current Model Applied to Gust Front	35
	6.4 Comparison of Detailed Structure of Gravity Currents and Gust Front	42
	6.4.1 Geometric Shape	43
	6.4.2 Internal Circulation and Gustiness	47
	6.4.3 Dynamic Similarity of Gust Front and Gravity Currents	51
7.	SUMMARY	54
8.	ACKNOWLEDGEMENTS	55
9.	REFERENCES	56

LIST OF FIGURES

Figure		Page
1	High density surface observation network and instrumented TV-tower facility operated by NSSL, Norman (NRO), Okla. in 1969. Network stations WKY, 2C, 5C, and 6A are identified as their records are used for illustrating the surface weather changes. The inset (upper right) shows the instrumented levels of the WKY-TV tower.	3
2	Sub-synoptic maps for 1800 CST, 31 May (a-f) and 0000 CST, 1 June 1969, (g-j). Figure 2a is the regular NWS surface station data for which analyses are shown in 2b, 2c, and 2d. In 2b isobars are drawn at 2-mb intervals. Isotherms and isodrosotherms shown in 2c and 2d, respectively, are at 5°F intervals. In both 2e and 2f height contours (decameters) are solid and isotherms (C) are dashed. The broad arrows in 2e indicate the dominate 850 mb currents and the area enclosed by the wavy line represents dew point temperatures in excess of 10°C. Figure 2g through 2j have the same conventions as 2a through 2d.	7
3	Sequence of frontal positions. The average propagation speed (m sec^{-1}) is shown within the time period spanned by the arrows. PJ denotes a pressure jump at the indicated time (CST).	9
4	Time sequence (CST) of the radar echoes of the 31 May 1969 squall line. The sequence was made from photographs of the PPI scope of the WSR-57 radar operating at 0 degrees elevation from Norman, Oklahoma (NRO). The echoes are contoured by different shades of grey beginning at a reflectivity factor threshold of 2×10^1 mm^6 m^{-3} and thereafter incrementing by factors of 10. Storm damage reports are located by X-marks and labeled. Each report, identified by identical labels, is described in table 1. Oklahoma towns near the damage reports are (from left-to-right) BTL(Butler), END (Enid), PNC (Ponca City), GRY (Geary), HNY (Hennessey), CRG (Carnegie), KFR (Kingfisher), CRS (Crescent), ABR (Amber), WKY-TV (instrumented TV tower in OKC), STW (Stillwater), CHR (Chandler), and TCH (Tecumseh).	11
5	Tracks (solid lines) of peak reflectivity elements of the echoes shown in figure 4. Dashed lines connect echo cores at regular time intervals. Bold numbers are the echo speeds (m sec^{-1}) averaged over 10-min periods. A, B, and C refer to the major thunderstorm echoes in figure 4.	14

Figure		Page
6	Time sequence (CST) of PPI radar displays showing the "thin line" echo and the trailing precipitation echoes at 0 degrees elevation. In the first picture (left) the range circles are at 25 n mile intervals, while the remaining four pictures have 10 n mile range circles. Distances between the echo boundary and the "thin line" are spanned by arrows. Units: nautical miles.	16
7	Major squall line features at 2337 1/2 CST. The PPI radar echo tracing is of the 2×10^1 and 2×10^4 mm^6 m^{-3} reflectivity factor contours. XY is the section line denoting the vertical plane used in the cross-section analysis of the gust front using WKY-tower data (figures 9 and 11); lines A_1B_1, A_2B_2, etc. indicate the location and orientation of the spatial sections shown in figure 10.	16
8	Sequence of the windshift (dashed) and gust-surge (solid) isochrones. The displacement speeds (m sec^{-1}) of the isochrone are shown.	18
9	Surface network and WKY-tower wind analyses. Section lines A_1B_1, A_2B_2, etc. in the surface network wind fields (figures 9a, 9c, 9e and 9g) show the orientations of the spatial variations of wind normal to the gust front (see figure 10). The space variations are obtained by transforming to space local time changes at the indicated surface stations. The points where the windshift and gust surge intersect these lines are denoted WS and GS, respectively. All the analysis in the X-Z plane through WKY (figures 9b, 9d, 9f and 9h) are aligned normal to the gust front and bounded by points X and Y as indicated in the network and tower fields. Corresponding features appearing in the network analysis and at the surface level of the vertical sections are denoted identically as shown.	19
10	Spatial variations of surface wind, pressure, and temperature normal to the gust front obtained by transforming analog measurements at stations WKY, 2C, 5A, and 6A to space. The pressure trend for WKY is shown (dashed). The segments A_1B_1, A_2B_2, etc. span the surface network as shown in figures 9, 11, and 12. The significant features labeled in the wind (figure 9), temperature (figure 11), and pressure (figure 12) fields are also indicated above. The significant points in the pressure and temperature profiles are: PJ-pressure jump, P_L-temporary leveling off period in the pressure curve, P_h-pressure head (P_h', if very weak), TB-temperature break, and T_L-temporary leveling off period in temperature curve. The position of heavy surface rain is "R".	24

Figure		Page
11	Network and tower temperature analyses: a) surface air temperature, b) surface wet-bulb potential temperature, and c) (next page) temperature cross section XY. Significant features are marked and labeled on the respective fields as before. See figure 10 for continuous temperature variations normal to the gust front along the cross sections indicated A_1B_1, etc.	25
12	Surface pressure analysis. The pressure values are deviations from the large-scale pressure trend (shown for WKY in figure 10). Significant features appearing in the wind speed analysis (figures 9e and 9f), temperature analysis (figure 11), and pressure curves (figure 10) are marked and labeled identically in the pressure field.	26
13	Schematic of the important analytical features of the wind and thermal structure of the windshift and gust front at WKY (upper). The surface pressure profile at WKY is also shown (lower).	29
14	Comparison of the observed and theoretical pressure jump of 31 May 1969. (a) Ambient and wet-bulb potential temperature profiles obtained from the 1800 CST TIK rawinsonde, modified in the lowest 500 m for the WKY tower conditions at 2300 CST. (b) Profile of the thermal inversion through the gravitational wave "jump" as obtained by application of Tepper's (1955) pressure jump model to the thermal inversion shown in (a). (c) Typical surface pressure profile through the observed pressure jump. (d) Computed hydrostatic pressure profile at the surface beneath the gravitational wave in (b). Windshift across the observed (e) and theoretical (f) pressure jump.	32
15	Vertical profiles of temperature and density at WKY just before and just after the gust surge passed, 2300 and 2345 CST, respectively.	33
16	(a) A saline "density current" (gravity current) propagating from right to left along the bottom of a transparent tank filled with pure water. Note the slightly elevated head and the turbulent mixing in its wake. (b) A saline current (flowing from left to right) revealing the formation of bulges which are swept backwards and roll up in the form of billows and then break up (after Simpson, 1969).	36

Figure		Page
17	Atmospheric gravity currents. (a) Cold front in Kansas (courtesy of Yih, 1969). (b) Haboob in Sudan (courtesy of Simpson, 1969). The Haboob is usually found just ahead of an active or dissipating squall line, but a few cases have revealed it to be associated with a strong dry cold front. In both (a) and (b) the front is moving from right to left.	38
18	Schematic flow model of a gravity current of density ρ_2 at the bottom of an infinitely deep reservoir of less dense fluid. Viewed with respect to a coordinate system attached to the gravity current, moving to the left with speed V, the dense mass is stationary while the environmental flow is toward the right at speed V.	39
19	A composite analysis of the wind field near the leading edge of a cold front in Australia (after Berson, 1958). The dashed and dotted curves represent zones of maximum vertical wind shear. These shear zones are assumed to correspond approximately to the frontal surfaces. Note the dip or level region in the shear profiles in the vicinity of 40 km from the leading edge of the front. The flow pattern is shown relative to a coordinate axis translating to the left along with frontal boundary. The streamlines are drawn roughly to fit the plotted wind vectors.	45
20	Internal circulation pattern of laboratory gravity currents as seen by a coordinate axis translating to the right with the speed of the head (after Middleton, 1966).	49
21	A composite schematic model combining the features of the analyzed and deduced structure of the windshift and gust front leading the squall line of 31 May 1966. (See the text for discussion).	48

LIST OF TABLES

Table		Page
1	Selected storm reports, times of wind damage and rainfall for 31 May 1969 squall line. Positions of reports relative to radar echoes are shown in figure 4.	12
2	Echo speed, size, intensity and duration prior to damage reports described in table 1. Storms are identified in figure 4.	13
3	Parameter values for calculation of theoretical gust front speed.	41

ABSTRACT

The structure of a severe gust front that preceded the squall line of 31 May 1969 is examined from measurements by the National Severe Storms Laboratory (NSSL) network of surface stations located in central Oklahoma. On the basis of the structure and the horizontal displacement of the cold outflow air mass, the mechanics of motion of the gust front is investigated.

In a vertical plane normal to the leading edge of the cold air current, the following structural features were revealed. The front edge of the profile of the air mass surface exhibited a projecting "nose" overlying the lagging front at the ground. The vertical extent of the cold air was greatest near the nose, i.e. 1700 m, while upstream the depth was constant at 1350 m. The vertical bulge near the nose is called a "head". The wind pattern with respect to a coordinate axis translating with the head at 20 m sec^{-1} displayed (a) a strong ambient air flow towards the nose which was lifted over the head (upward velocities at the 400 m height of the nose were up to 2.5 m sec^{-1}), (b) a closed circulation cell within the head, dominated by a high-speed forward current along the bottom as exhibited by a 13 m sec^{-1} current only 180 m above the ground. Upstream cold air flowed into the head circulation field, apparently maintaining the cold air against erosion effects resulting from (c) turbulent entrainment of ambient air below the nose and, more important, in the wake of the head crest. These structural features are remarkably similar to analogous characteristics of gravity currents in stratified fluids produced in laboratory experiments.

The gust front was approximately dynamically similar to theoretical and experimental gravity currents. In this regard, it is speculated that high horizontal momentum air in the thunderstorm downdraft, injected into the outflow current, tends to increase the gust front's propagational speed; thus, its internal Froude number is greater than if gravity were the only motive force. However, the analysis indicates this effect was small in the 31 May case.

GRAVITY CURRENT MODEL APPLIED TO ANALYSIS OF SQUALL-LINE GUST FRONT[1]

Jess Charba[2]
University of Oklahoma

1. INTRODUCTION

Air transportation has been mushrooming during recent years, and the increasingly serious air traffic congestion problem near airports is often aggravated by the potential danger posed by the cold outflow from a nearby thunderstorm. Aviators commonly agree that the strong low-level wind gusts and the extreme wind shears that characterize this air mass pose a serious hazard to aircraft in their landing or take-off patterns. This problem has recently spurred some meteorologists to a renewed interest in this severe wind phenomenon (Fujita, 1966; Barclay and Wilk, 1970; Sasaki, 1970; and Colmer, 1971). Because of its characteristic gusty winds, this cold outflow air mass has been called a gust front by the above researchers. In this paper the term gust front is adopted for general reference to this cold air mass.

A scan of the meteorological literature for documented studies on the severe low-level winds associated with thunderstorms points up a need for further investigation. Byers and Braham (1949) made detailed analyses of the surface wind fields of an assortment of convective storms in Florida and Ohio and were among the first to note the potential danger such winds pose to aircraft. Barclay and Wilk (1970) and Sasaki (1970) emphasized the structural aspects of severe surface wind fields revealed by objective analysis of several squall-line cases. Fujita (1966) examined the turbulence structure of a squall-line gust front in the layer 1 to 2 km above the ground. Colmer (1971) investigated a few key features of the structure of the initial gust in the surface-to-500 m layer in 13 gust-front cases. However, a need remains for a complete definition of the structure of kinematic and thermodynamic variables in three dimensions. Furthermore, for improved forecasting of the gust front, it will be necessary to obtain a better understanding of the mechanism of formation and maintenance of the gusty air mass and to clarify the mechanics of its horizontal propagation outward from the parent storm.

This study is a detailed analysis of the structure and horizontal propagation of the severe gust front connected with the squall line of 31 May 1969. The wind and thermal fields of the outflow air mass are

---

[1]Supported by NOAA Grant No. E22-43-70G through the Environmental Research Laboratories' National Severe Storms Laboratory, this research also is reported slightly revised as a thesis in partial fulfillment of the requirements for the PhD in Meteorology at the University of Oklahoma.

[2]Present affiliation: National Weather Service, Techniques Development Laboratory, Silver Spring, Maryland.

analyzed in three dimensions. Important features of these fields are compared with corresponding fields of gravity currents formed in laboratory tank experiments (Keulegan, 1958; Middleton, 1966; and Simpson, 1969) and in a numerical simulation (Daly and Pracht, 1968). The investigation touches on the mechanism of formation of the gust front as well as the mechanism involved in its subsequent maintenance during a horizontal displacement of about 100 n miles. The dynamical relations between the horizontal momentum of the air mass and the horizontal hydrostatic pressure gradient across the frontal surface is examined. The clarification of these aspects is attempted by applying the theory of gravity currents formulated by von Kårman (1940), Prandtl (1952), and Benjamin (1968) to the analytical structure of the gust front. Results of simple applications are then compared with experimental observations of gravity currents.

To the author's knowledge, such an investigation of the cold air outflow of thunderstorms has not appeared in the literature. This is undoubtedly due mainly to the scarcity of high resolution measurements, especially in the vertical direction. On the other hand, similar investigations (but in less detail) have been made of larger scale atmospheric gravity-type flows, e.g., sea-breeze fronts and the leading edge of cold fronts (Berson, 1958; Clarke, 1961; and Simpson, 1969). This study considers some of the fundamental similarities and differences between the structure and dynamic character of these phenomena and the gust front.

2. METHODS OF DATA PROCESSING AND ANALYSIS

2.1 Special Data Used

The analysis of the squall-line gust front used measurements from NSSL's high density network of surface stations and the instrumented WKY-TV tower shown in figure 1. The average distance between adjacent surface stations in 1969 was 9 km. Surface wind, pressure, temperature, relative humidity, and rainfall measurements were automatically recorded at each station on strip charts in analog form. NSSL maintenance personnel took a great degree of care in 1969 to insure instrument calibration to meet National Weather Service (NWS) standards and chart time accuracy to $\pm$ 1 min. Instruments at seven levels on the tower recorded wind and temperature measurements to a maximum height of 444.4 m (see Carter, 1970, for complete description). Accuracy of the tower records easily exceeded the requirements for this analysis.

NSSL made available radar scope photographs of the horizontally scanning WSR-57 and vertically scanning MPS-4. The PPI (plan-position indicator) of the WSR-57 and the RHI (range-height indicator) of the MPS-4 were photographed at 1-min intervals. This radar coverage, to a maximum range of 100 n miles around Norman, Oklahoma (NRO), gave a complete picture of the development and approach of the squall line toward the surface station network from the west-northwest. Volunteer observer reports and Storm Data tabulations of severe weather and damage inflicted by the thunderstorms were used with the radar pictures for

identification of severe echoes. Each year NSSL sends standard checklist forms to about 400 volunteer observers within the area of radar coverage. Although just how many persons receiving the forms respond to them is unknown, the large number of reports received by NSSL combined with additional reports compiled in Storm Data gives reasonable assurance that large, severe storms were not missed. The severe weather reports are described in table 1 (page 12) and are related to storm echoes in table 2 (page 13).

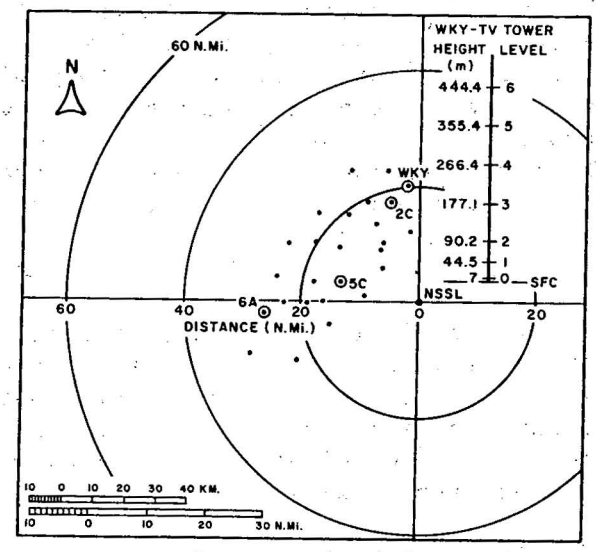

Figure 1. High density surface observation network and instrumented TV-tower facility operated by NSSL, Norman (NRO), Okla. in 1969. Network stations WKY, 2C, 5C, and 6A are identified as their records are used for illustrating the surface weather changes. The inset (upper right) shows the instrumented levels of the WKY-TV tower.

2.2 Data Extracting and Smoothing

The pressure and wind data extracted from the analog charts were smoothed to remove small-scale random variations. For the station pressure, the microbarogram was digitized at 1.25-min intervals and then smoothed by the application of a three-point "hanning" filter designed to remove waves whose periods are less than 2.5 min (or 3 km wavelength).[3] The wind records were smoothed by hand in accordance with the criterion of removing waves of periods up to 2.5 min. These smoothed data define the "characteristic" pressure and wind of the gust front.

During the gust-front passage, the wind speed records exhibited large amplitude fluctuations. At any analysis time, the maximum and/or minimum wind speed was defined as an average of the consecutive speed peaks and/or consecutive speed minima, over an interval of 2.5 min centered at the analysis time. These maximum and minimum wind speed data are used as a measure of the wind gustiness (discussed later).

2.3 Time-to-Space Conversions

Conversions of chart records from the time to the space dimension were employed in the analysis of both the network and tower measurements.

[3]The short-term transformation from the time to the space domain assumes steadiness of the measured gust-front parameters over the short time interval involved.

The method is discussed by Fujita (1963) and employed in network analysis by Charba and Sasaki (1971). This method of using continuous measurements at a station for extrapolation to points between stations was found to be necessary for accurate analysis of wavelengths as short as 12 km. The conversion from the time to the space dimension was similarly applied to WKY tower records to implement the analysis of the wind and thermal structure of the gust front in a vertical plane section.

2.4 Special Analysis Techniques

The analysis of parameters derived from the wind measurements and the method used to analyze the surface pressure field require elaboration. Discussed first are the procedures used to obtain the divergence and streamline fields of the surface wind and the stream function and gustiness fields of tower winds in a vertical plane normal to the leading edge of the gust front (x-direction).

The computation of the surface wind divergence employed a rectangular grid whose spacing was 5 km. The wind direction and speed were interpolated at grid-point locations from isogon and isotach patterns. The horizontal velocity divergence at grid point i,j is computed according to

$$Div_{i,j} = (u_{i+1} - u_{i-1} + v_{j+1} - v_{j-1})/2d, \qquad (1)$$

where d is the grid spacing, while u and v are the respective wind components normal (x-direction) and tangent (y-direction) to the leading edge of the gust front; i increases by 1 as x increases by d, and likewise for j in the y-direction.

Streamline patterns were constructed both at the surface and in the vertical plane defined above. The streamlines representing the surface flow pattern were constructed entirely by hand from a field of plotted wind vectors. The computation of the stream function field was valid in the x-z plane near the gust surge since $\partial v/\partial y$ was an order of magnitude smaller than $\partial u/\partial x$ at the surface level. If we assume that $\partial v/\partial y$ is negligibly small compared with $\partial u/\partial x$ everywhere in the vertical plane from the surface to 444 m, the mass continuity equation for incompressible flow becomes

$$\frac{\partial u}{\partial x} + \frac{\partial w}{\partial z} = 0, \qquad (2)$$

where the vertical velocity component, w, is positive in the upward (z) direction. Following Clarke (1961) a stream function, ψ, satisfying (2) is defined by

$$u = -\frac{\partial \psi}{\partial z} \qquad (3a)$$

$$w = \frac{\partial \psi}{\partial x}. \tag{3b}$$

Since u is known as a function of height, h, in the x-z plane from tower winds, the ψ-field is computed by

$$\psi = - \int_0^h u dz. \tag{4}$$

After ψ has been computed w can be obtained from (3b).

The gustiness, G, of the network and tower winds is defined by

$$G = \overline{V}_{max} - \overline{V}_{min},$$

where $\overline{V}_{max}$ and $\overline{V}_{min}$ are the respective 2.5-min averages of consecutive peak and minimum wind speed data (discussed earlier). Thus, the gustiness represents the magnitude of wind speed fluctuation, i.e., gusts, about the characteristic wind speed.

The analysis of surface pressure employed a special method that removes instrument calibration errors, eliminates the necessity of reducing the pressure to a common reference level, and separates the mesoscale disturbance from larger scale pressure changes. The removal of these problems for a particular station is accomplished at once by determining the actual station pressure trace representing large-scale variations, i.e., wavelengths $>$ 500 km. The latter pressure curve, called the trend (Charba and Sasaki, 1971), is subtracted from the original pressure curve. The resulting pressure deviations from the trend represent the mesoscale disturbances in the approximate wavelength range of 5 to 500 km. The entire process of obtaining the mesoscale pressure variation at a station for a particular analysis time is accomplished in four steps; (1) the original trace is digitized at 45-min intervals over 24 hours centered on the storm event, (2) the resulting discrete data set is smoothed by a centered nine-point moving average operator (this operator effectively removes waves with periods 12 hr and less), (3) a linear interpolation obtains the pressure trend value for an analysis time between the smoothed points, and (4) the interpolated pressure trend value is subtracted from the corresponding ambient pressure value (previously smoothed only to remove small-scale variations). This process is repeated for each network microbarogram to obtain the pressure deviations for all stations.

2.5 Concluding Comments on Analysis Approach

All the data extraction and much of the processing was performed manually; however, objective criteria and techniques were established and employed as periodic checks to insure a relatively high degree of objectivity. Of course, the disadvantage inherent in the hand process is the tedious work required. This disadvantage is, to a great degree, compensated for by the more effective use of the experience and insight of the analyst in detecting key subtle features in the data records that might be unnoticed or smoothed out if fully automated techniques were used. Such is the case in an analysis where little is known about the phenomenon before the investigation. This gust front analysis certainly falls into the above category.

3. EVOLUTION OF SQUALL LINE WITHIN LARGE-SCALE WEATHER PATTERN

3.1 Synoptic

The synoptic pattern that spawned the convective outbreak in the Southern Great Plains was typical for severe storms in that region. At 1800 CST, 31 May 1969 a vigorous late-season cold air mass was pushing southeast across Colorado, Kansas, and Iowa behind a deep, closed low pressure center located just west of Lake Superior. A low pressure trough extended southwest from the low to El Paso, Texas, at all tropospheric levels.

3.2 Sub-Synoptic

The sub-synoptic pattern at 1800 CST is revealed in figure 2 a-f. At the surface and 850 mb, a warm, moist southerly current meets the northerly cold-air surge over extreme northwest Oklahoma to eastern Kansas. Hot, dry air from west Texas was drifting towards eastern Kansas. The implied differential thermal and moisture advection in the vertical direction created a potentially unstable stratification as indicated by lifted index values of -3 and -4 at Dodge City (DDC) and Oklahoma City (OKC).

Several mechanisms over western Oklahoma and Kansas evidently provided the upward air-motion that unleashed the potential instability. Among them was the mechanical lifting provided by the undercutting cold air mass. Figure 3 shows that the southward displacement speed of the front increased from 8.5 to 16.0 m sec^{-1} across Colorado and the Texas panhandle during the afternoon and evening of 31 May. Certainly mechanical lifting was substantial in this area in the face of the southward cold-frontal push. Upward motion also occurred ahead of the front over the Texas panhandle and western Oklahoma in connection with convergence of the 850-mb flow into a low pressure area (div = -1.5×10^{-4} sec^{-1}) and divergence of the 500 mb flow ahead of a short wave trough (div = 1.4×10^{-4} sec^{-1}) in that area. Upward motion was further aided in the area by a topographical upslope flow.

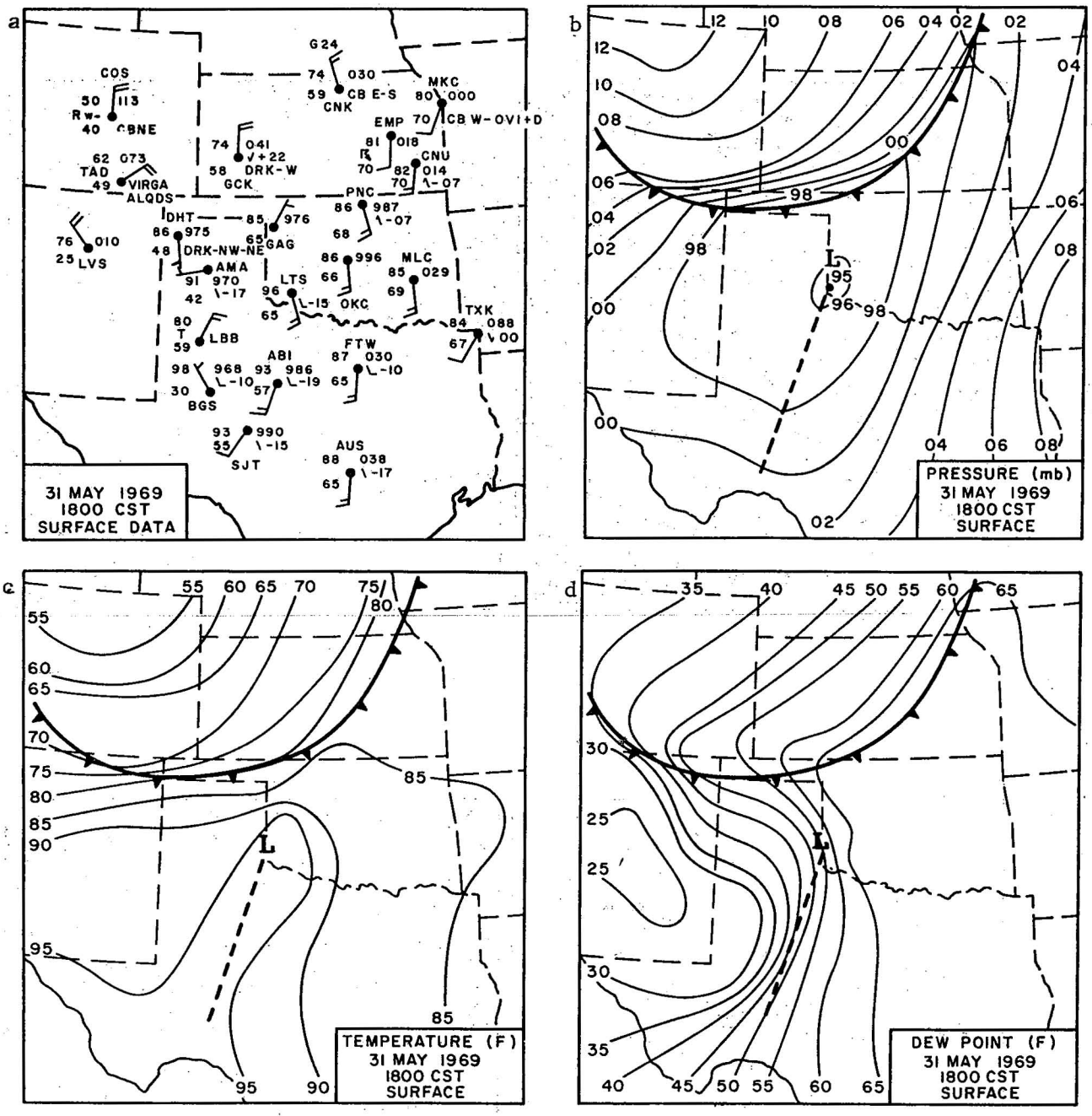

Figure 2. Sub-synoptic maps for 1800 CST, 31 May (a-f) and 0000 CST, 1 June 1969, (g-j). Figure 2a is the regular NWS surface station data for which analyses are shown in 2b, 2c, and 2d. In 2b isobars are drawn at 2-mb intervals. Isotherms and isodrosotherms shown in 2c and 2d, respectively, are at 5°F intervals. In both 2e and 2f height contours (decameters) are solid and isotherms (C) are dashed. The broad arrows in 2e indicate the dominant 850 mb currents and the area enclosed by the wavy line represents dew point temperatures in excess of 10°C. Figure 2g through 2j have the same conventions as 2a through 2d.

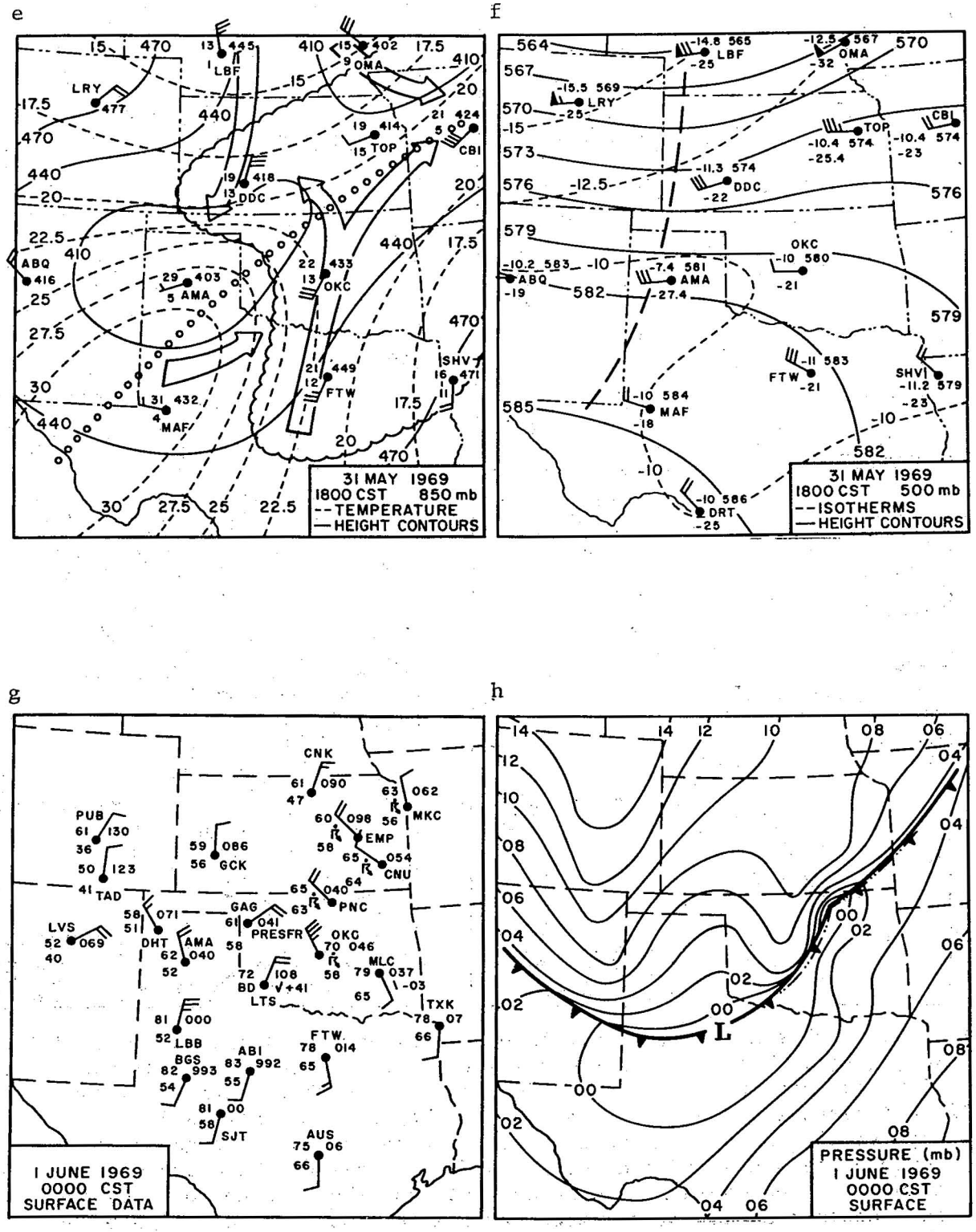

Figure 2 (Continued)

i

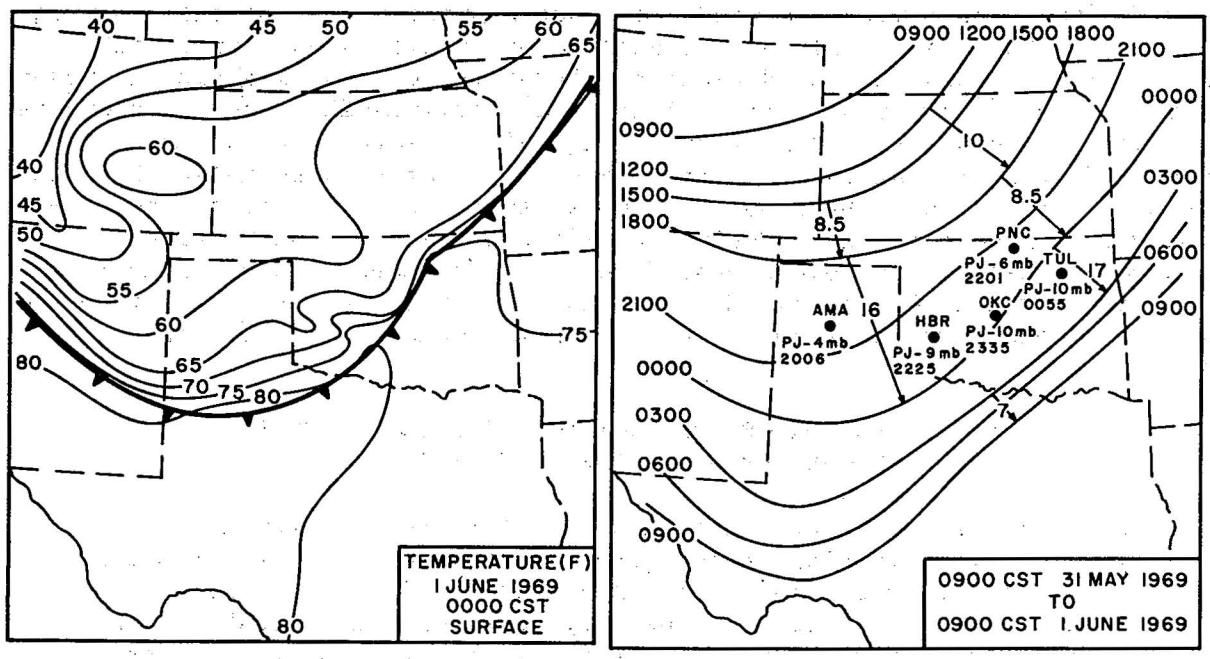

j

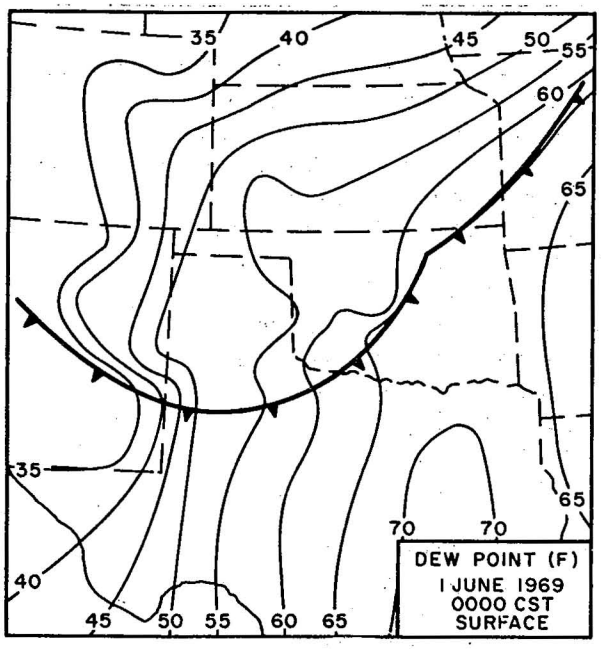

Figure 2 (Continued)

Figure 3. Sequence of frontal positions. The average propagation speed (m sec^{-1}) is shown within the time period spanned by the arrows. PJ denotes a pressure jump at the indicated time (CST).

Thunderstorms made an initial appearance near the cold front in the extreme northwest panhandle of Oklahoma and southwest Kansas at about 1600 CST according to NWS radar summaries. A squall line rapidly formed and moved east at 15 to 20 m sec^{-1}. This speed is significantly greater than the mean wind speed in the troposphere, as revealed by two TIK (Tinker Air Force Base in Oklahoma City) soundings, 1800 CST 31 May and 0600 CST 1 June, displaced 6 hr from the 0000 CST 1 June squall-line passage over the rawinsonde site. The mean wind vector revealed by these soundings had a magnitude of 10 m sec^{-1} from 262°. The 5 to 10 m sec^{-1} discre-

pancy between the mean wind and the propagational speed of the cumulonimbi suggests that the rawinsonde winds were not representative of the steering wind ambient to the squall-line thunderstorms. This is not surprising since a mesocyclone developed along the front in western Oklahoma and moved rapidly across the northern part of the state (figure 2h). The radar echoes embedded in the high-speed southern "wing" of the wave moved about 8 to 10 m sec^{-1} faster than those to the north, in apparent association with the cyclonic circulation. By 0000 CST, the southern extension of the squall-line wave passed over the OKC-NRO area (figure 2g-j). A heavy rain area was preceded by a severe gust front that produced wind gusts up to 35 m sec^{-1} at the WKY tower. Note the intense pressure and temperature gradients normal to the squall line in central Oklahoma in figures 2h and 2i.

4. EVOLUTION OF THE SQUALL-LINE THUNDERSTORMS AND GUST FRONT THAT ENTERED THE NETWORK

The analysis and interpretation of the network measurements were greatly aided by an initial investigation of the temporal variations in certain gust-front properties. This required the identification of the parent echo (which for a squall line, may be a formidable task) so that the temporal and spatial variations of the intensity and propagational character of both the gust front and the parent thunderstorm could be described before the analysis.

4.1 Echo Patterns and Related Wind Damage

Thunderstorms whose echoes are organized in a wave pattern are often severe. Nolen (1959) was first to recognize and define the line-echo-wave pattern (LEWP) as an echo feature often associated with occurences of tornadoes. Cook (1961) found that tornadoes are most likely to occur within 50 n miles south of the center of the fast-moving ($\geq$ 40 kt) LEWP, particularly when the line is scattered or broken. Severe windstorms predominate in the same area when the line is solid.

For the 31 May - 1 June squall line, a distinct LEWP developed in western Oklahoma in apparent association with the mesocyclone discussed earlier. In figure 4 a-c notice how the fast-moving echo A overtakes B during 2130-2300 CST; thereafter A and B eventu~~ally~~ amalgomate. At the same time, echo A grew continuously along its southern tip, and by 2330 CST a solid echo line extended 60 n miles to the south of the point of amalgomation of A and B. While A and B were merging, A accelerated eastward relative to B, thus forming the LEWP. The relative vorticity within the echo wave, calculated from the differential displacements of peak reflectivity elements during 2255-2335 CST (figure 5) was $+5.4 \times 10^{-4}$ sec^{-1}. On the other hand, storm C was obviously not part of the LEWP to the north of it and showed no wave configuration of its own.

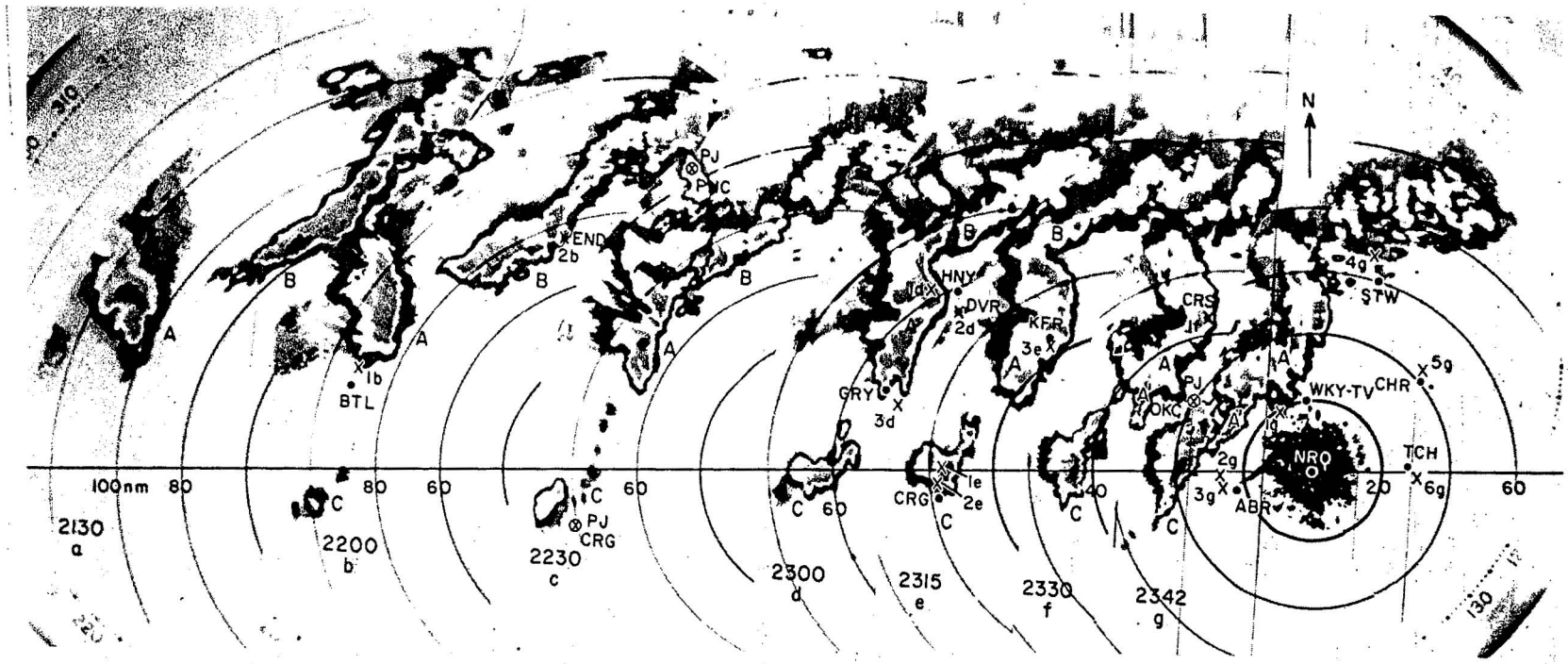

Figure 4. Time sequence (CST) of the radar echoes of the 31 May 1969 squall line. The sequence was made from photographs of the PPI scope of the WSR-57 radar operating at 0 degrees elevation from Norman, Oklahoma (NRO). The echoes are contoured by different shades of grey beginning at a reflectivity factor threshold of 2×10^{1} mm^{6} m^{-3} and thereafter incrementing by factors of 10. Storm damage reports are located by X-marks and labeled. Each report, identified by identical labels, is described in table 1. Oklahoma towns near the damage reports are (from left-to-right) BTL (Butler), END (Enid), PNC (Ponca City), GRY (Geary), HNY (Hennessey), CRG (Carnegie), KFR (Kingfisher), CRS (Crescent), ABR (Amber), WKY-TV (instrumented TV tower in OKC), STW (Stillwater), CHR (Chandler), and TCH (Tecumseh).

Table 1. Selected storm reports, times of wind damage and rainfall for 31 May 1969 squall line. Positions of reports relative to radar echoes are shown in figure 4.

Rept. No.	Quoted Remarks of Volunteer Observers	Damaging Wind			Rain		
		Began (CST)	Ended (CST)	Dir.	Began (CST)	Ended (CST)	Amt (in.)
1b	Considerable damage to limbs of trees. Some damage to cotton and barley crops due to strong NW wind. Considerable blowing dust.	2200	0030	NW	--	--	0
2b	Winds were clocked up to 65 mph. Significant damage to trees and crops.	2200 (?)	0000	?	2200	0000	1.78
1d	Some trees uprooted and outbuildings damaged; gardens were flattened.	2245	0000	NW	2255	?	3.00
2d	Severe damage to vegetation. Every large tree suffered some limb breakage. Several large trees were blown over. Several trailer houses were severely damaged. Three persons received minor injuries.	2300	?	?	?	?	?
3d	Wind estimated 65-75 mph. Damage to barn two miles north. Storms raged for several hrs 20-40 mile N of us.	2300	2310	N	?	?	0.20
1e	Three persons were injured in overturned camper trailer.	2300	?	?	?	?	?
2e	Hail 3/4 inches in diameter 2313-2320. No wind report.	?	?	?	2313	2320	0.30
3e	Tree-limb damage everywhere.	2310	?	NW	2316	2345	0.60
1f	Had 1/2 inch diameter hail during 2331-2333 CST. Little damage to trees(?)	2321	2340	W-NW	2333	2337	0.80
1g	Light damage to trees and utility lines in north and west OKC. Peak wind gust measured on WKY-TV tower was 76 mph.	2330	2345	NW	2345	--	--
2g	Wind estimated 60-65 mph. Little damage to trees and crops.	0000	0020	N-NE	0030	0050	0.50
3g	Hail 1/4 inches in diameter fell between 0000-0010. Little damage to crops by wind.	0010	0100	W-NW	?	?	0.30
4g	Little damage to trees.	0020	0100	NW	0030	0100	2.10
5g	Some leaves and branches broken off trees but damage was relatively small.	0030	0200	NW	0100	0245	0.40
6g	Little damage to trees by wind.	0050	0110	?	0118	0140	0.60

Table 2. Echo speed, size, intensity and duration prior to damage reports described in table 1. Storms are identified in figure 4.

Storm	Rept. No.	Time (CST)	Translation Speed (kts)	Dia. (nm)	Height (kft)	Reflectivity Factor (dbZ)[1]	Prior Duration (hrs)
A	1_b	2200	20	20	54	52	2
B	2_b	2200	15-20	20	49	52	2
A	1_d	2245	25	25	51	45	3
A	2_d	2255	28	25	50	47	3
A	3_d	2300	21	20	48	48	3
C	1_e	2310	24	17	48	55	1 1/4
C	2_e	2310	24	17	48	55	1 1/4
A	3_e	2310	30	23	46	45	3 1/4
A	1_f	2321	25	19	48	39	3 1/2
A	1_g	2330	20	18	45	42	3 3/4
C	2_g	0000	20	18	48	50	1 3/4
C	3_g	0010	20	18	48	50	1 3/4
A	4_g	0020	-	Missing	-	-	-
A	5_g	0030	-	"	-	-	-
A	6_g	0050	-	"	-	-	-

[1] Zero degrees elevation, $p_{dbZ} = 10 \log \frac{Z}{(1 \times 10^{\circ})}$, Z--reflectivity factor

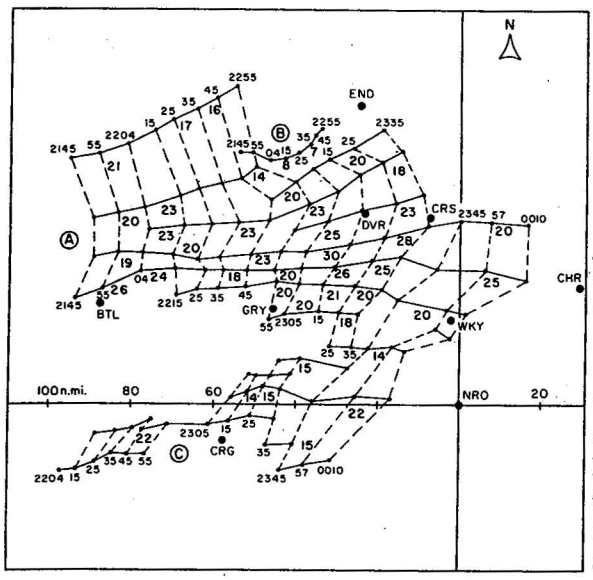

Figure 5. Tracks (solid lines) of peak reflectivity elements of the echoes shown in figure 4. Dashed lines connect echo cores at regular time intervals. Bold numbers are the echo speeds (m sec^{-1}) averaged over 10-min periods. A, B, and C refer to the major thunderstorm echoes in figure 4.

Virtually all the severe wind damage appeared to be associated with the protruding wing of the LEWP, i.e., echo A, in agreement with the findings of Cook (1961). This is established from the volunteer observer and Storm Data wind damage reports compiled in table 1. Greatest wind damage was reported from the Dover (DVR) area (report number 2d in table 1 and fig. 4). Notice that the leading edge of the protruding echo of the LEWP was just west of DVR when the high winds began. Quite in contrast, storm C apparently imparted relatively little wind destruction during the period spanned in figure 4.

4.2 Echo Characteristics and Related Wind Damage

Focusing on the individual echoes within the squall line, a definite correlation appears between certain echo properties and the severity of the wind damage. Table 2 lists the translation speed, prior active duration, echo diameter, height of top, and reflectivity of the echo that passed over the point of reported wind damage. The echo property having the clearest correlation to the wind damage is the translation speed. In figure 5 the echo speeds are indicated in bold numbers (m sec^{-1}) below paths of peak reflectivity elements. When we compare this speed pattern with the damage pattern (table 1 and figure 4), it is generally seen that the greater the rate of echo displacement the greater the wind damage and vice versa. Note the especially high echo speeds of 25 to 30 m sec^{-1} in the DVR area. Colmer (1971) observed a similar relationship from a plot of maximum wind gust versus echo speed obtained from 13 gust-front cases within the NSSL network in 1969 to 1970. The remaining parameters in table 2 also generally reveal a parallel between their magnitudes and the severity of the wind damage. Using these relationships as criteria, we infer from figure 4 and table 2 that echo A (LEWP) was in the mature stage during 2300 to 2315 CST but began to weaken by 2342 CST (figure 4g) just before it entered the NSSL surface network.[4] This observation agrees with the

[4]The appendage at the southern tip of echo A, i.e., echo A', made an initial appearance in the preceding picture and is not considered to be part of echo A or the LEWP.

reports of lesser wind damage downwind from A's 2342 CST position. On the other hand, storm C, which entered the southwestern part of the network, was in its mature stage at 2342 CST but at no time indicated winds as strong as those associated with echo A.

4.3 Origin and Evolution of the Gust Front Entering the Network

The severe gust front that entered the surface network at 2320 CST appears to have originiated from echo A. This is suggested by a time sequence of positions of a "thin line" radar echo (figure 6) and the direction of the cold outflow current with respect to the precipitation echoes (figure 7). During the period it traversed the network, the thin line was consistently found at the leading edge of the gust front. (This relationship between a radar thin line and a surface cold front has previously been observed by Lidga and Bigler, 1958; and Fujita, 1966). Assuming such a correspondence existed before the gust front entered the network the orientation of the thin line gives a clear impression that the gust front emerged from echo A (figure 5). This agrees with the streamline pattern of the surface network winds. (The analysis is shown in the next section.)

Quite typically the forward edge of the cold outflow air mass of thunderstorms lies within several miles of the main rain area when the convective cells are in the initial part of the mature stage, but lies as much as 20 to 30 n miles ahead of the parent storms during the latter part of their mature or dissipating stage (Byers and Braham, 1949; Colmer, 1971). Figure 4 and table 2 demonstrate that during the mature stage of echo A, i.e., 2300 to 2315 CST, damaging winds occurred within 5 n miles of the forward echo boundary. On the other hand, as the squall line approached and crossed the NSSL network, the forward gust-frontal boundary was increasing its lead over the forward echo boundary from 8.5 to 12.0 n miles (figure 6).

4.4 Concluding Remarks

Although this analysis of the gust-front's history is based on relatively crude data, the findings discussed above, when logically integrated, yield a rather complete description of the gust front before and during its passage over the network. The main source of the gust front was echo A. The gust front became well organized and quite severe as echo A attained high forward speed during the development of the LEWP. Later, as the parent A echo decelerated somewhat, the gust front pushed ahead of it. By the time the southern extremity of the LEWP had reached the northern part of the NSSL network, the echoes were in the "late mature" stage and the gust front had moved to a position of about 10 n miles downstream from the echo's forward boundary. This distance increased only slightly as the squall line passed over the network. It is important to point out (as will be seen in the last chapter) that while the gust front, swept over the entire network, echo A barely skirted its northern boundary echo. The major part of the network was

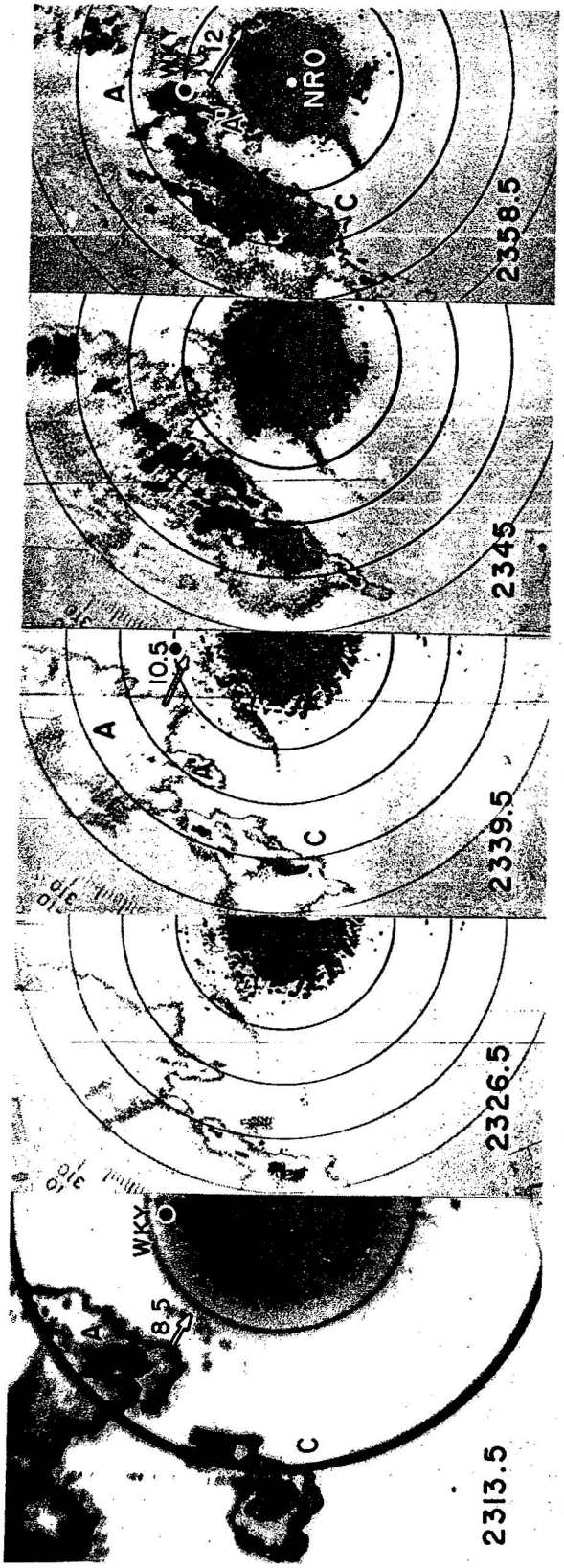

Figure 6. Time sequence (CST) of PPI radar displays showing the "thin line" echo and the trailing precipitation echoes at 0 degrees elevation. In the first picture (left) the range circles are at 25 n mile intervals, while the remaining four pictures have 10 n mile range circles. Distances between the echo boundary and the "thin line" are spanned by arrows. Units: nautical miles.

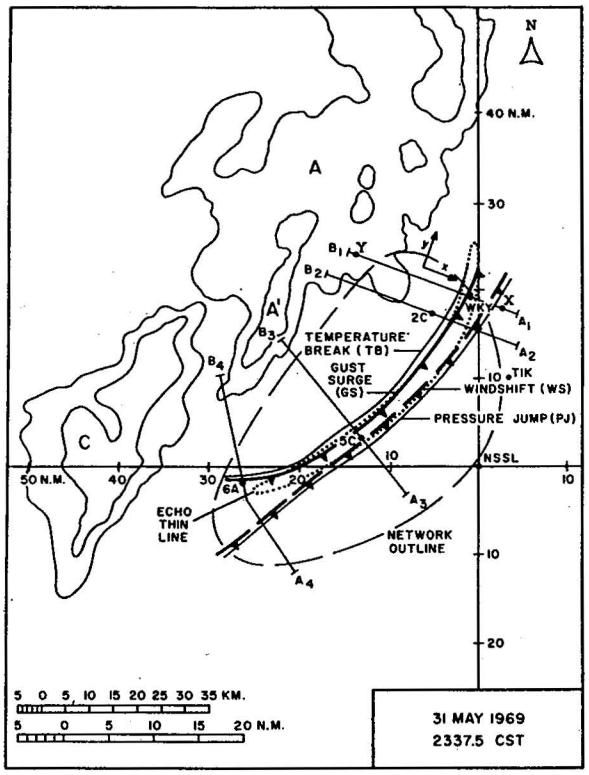

Figure 7. Major squall line features at 2337 1/2 CST. The PPI radar echo tracing is of the 2×10^1 and 2×10^4 mm^6 m^{-3} reflectivity factor contours. XY is the section line denoting the vertical plane used in the cross-section analysis of the gust front using WKY-tower data (figures 9 and 11); lines A_1B_1, A_2,B_2, etc. indicate the location and orientation of the spatial sections shown in figure 10.

traversed partly by newly developed echoes along the southern tip of echo A and partly by echo C; both echoes were characterized by surface wind of less severity than those produced by the original A echo.

5. ANALYTICAL STRUCTURE OF THE THUNDERSTORM OUTFLOW LEADING THE SQUALL LINE

The width of the gusty outflow leading the squall line precipitation echoes was only slightly less than the width of the network. The time period that the network encompassed the entire air mass was quite short. Consequently, an analysis of the whole air mass was possible at only one time. Since time-to-space transformations of data measurements were necessary in the analysis, the validity of the assumption of steadiness of the gust front and echo properties had to be investigated beforehand. In the preceding chapter the broad-scale temporal and spatial changes of the morphology and propagation of the gust front and precipitation echoes were examined for the period spanning the approach and passage over the network. Here we focus on the smaller scale characteristics of these aspects while the outflow was passing over the network. Following this brief survey, the analytical structure of outflow is discussed in detail.

5.1 Displacement Character of Squall System

Two distinct surface wind change lines were featured between the uniform, warm southerly flow and the cold, gusty northwesterly current of the squall-line outflow. The initial discontinuity was an abrupt wind direction change from uniform southerly to northwesterly. The line along which this shift in direction occurred is called the windshift line (figure 7). Note in figure 7 that a "pressure-jump line," i.e., a line marking the leading edge of a steep pressure rise, was practically coincident with the windshift line. Following the windshift and pressure-jump lines in figure 7 is a line marking an intense surge in the speed and gustiness of the wind; this wind-surge line is called the gust surge. Note that the temperature "break" line (TB in figure 7), marking the leading edge of a sharp temperature fall, lies parallel to and several kilometers behind the gust-surge line.

At 2337 1/2 CST the windshift and gust surge were separated by 5 km at WKY, but over the entire network the average distance was 8 km (figure 7). The radar thin line occupies the strip between the windshift and gust-surge lines.[5] The wind change lines near WKY lie about 19 km ahead of the forward boundaries of echoes A and A'.

[5] In the preceding chapter the thin line was used to locate the position of the gust-surge line before the gust front entered the network. The slight difference in the positions of the thin line and gust surge introduces negligible error into the former consideration.

Significant differential displacements among the echo boundary, gust surge, and windshift occurred from 2313 1/2 to 2358 1/2 CST. If we assume the position of the gust surge is well approximated by the thin line during this period (as it was during the entire period that both were over the network, i.e. 2325 to 2350 CST), figure 6 shows the gust surge to increase its lead over the echo boundary from 8.5 n miles (15 km) to 12.0 n miles (22 km) during 2313 1/2 to 2358 1/2 CST. A sequence of isochrones of the thin-line positions (not shown) indicated the gust surge maintained a practically steady displacement speed of 22 m sec^{-1} during this period. At the same time, the echo boundary propagated steadily at 19 m sec^{-1}. On the other hand, the gust surge had a substantially greater displacement speed than the windshift while both were over the network. The sequence of isochrones of the windshift and gust surge positions in figure 8 show this; in the vicinity of WKY, the displacement of the gust surge had a speed of 21 m sec^{-1} compared with the windshift's 15 m sec^{-1}.

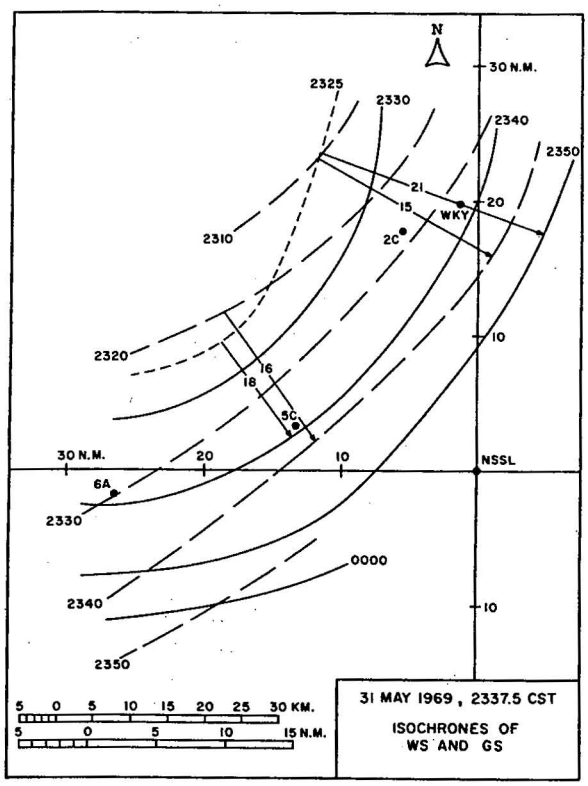

Figure 8. Sequence of the windshift (dashed) and gust-surge (solid) isochrones. The displacement speeds (m sec^{-1}) of the isochrone are shown.

Thus, the echo boundary and the gust surge maintained a steady eastward translation in the 45-min before and during passage over the network, although the gust surge moved 3 m sec^{-1} faster than the echo. The windshift moved 6 m sec^{-1} slower than the gust surge; this difference was taken into account in the transformations from time to the space domain and accounts for the space scale discontinuity near 10 km in the vertical cross section (figures are discussed subsequently). Based on the observed speeds of the echo boundary and gust surge, the velocity of the gust front employed in the scale conversions was 20 m sec^{-1}.

5.2 Analytical Structure

5.2.1 Windshift

Byers and Braham (1949), Fujita (1966), and Colmer (1971) have reported that a wind direction change often precedes the severe gust front. On 31 May 1969, the windshift was quite distinct, as illustrated in figure 9a

Figure 9. Surface network and WKY-tower wind analyses. Section lines A_1B_1, A_2B_2, etc. in the surface network wind fields (figures 9a, 9c, 9e and 9g) show the orientations of the spatial variations of wind normal to the gust front (see figure 10). The space variations are obtained by transforming to space local time changes at the indicated surface stations. The points where the windshift and gust surge intersect these lines are denoted WS and GS, respectively. All the analysis in the X-Z plane through WKY (figures 9b, 9d, 9f and 9h) are aligned normal to the gust front and bounded by points X and Y as indicated in the network and tower fields. Corresponding features appearing in the network analysis and at the surface level of the vertical sections are denoted identically as shown.

a

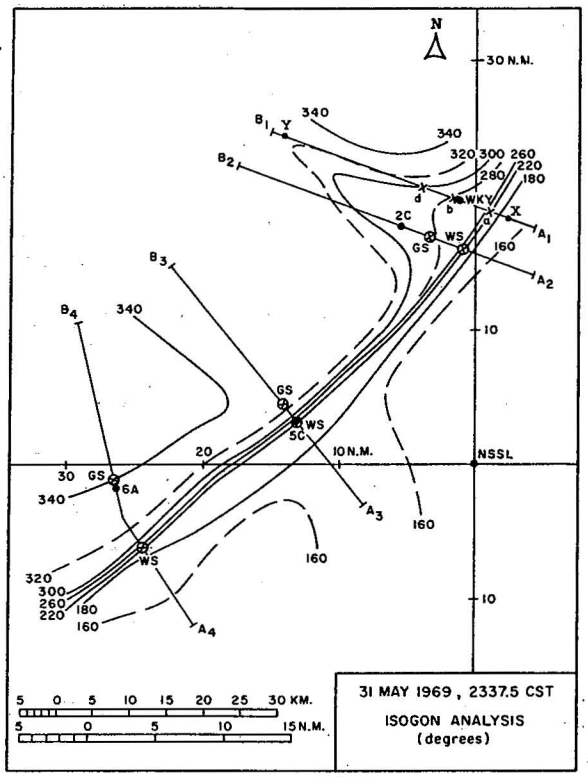

b

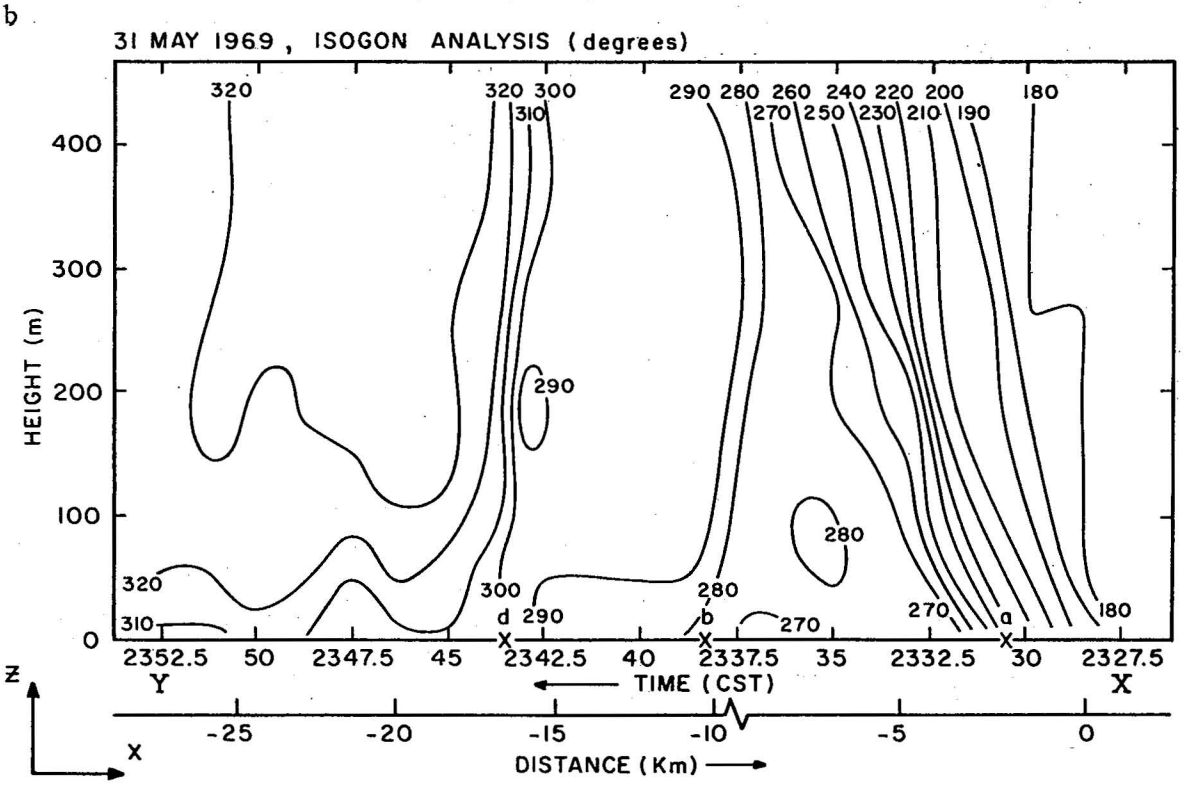

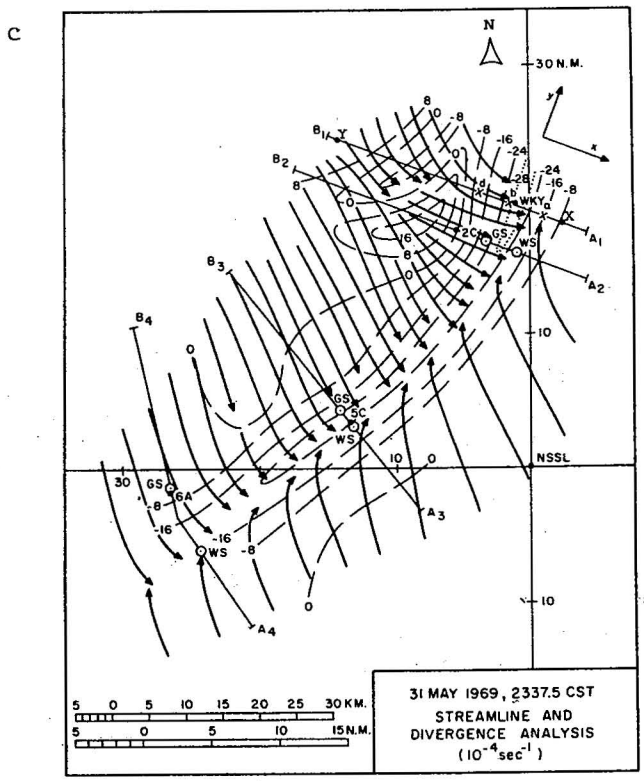

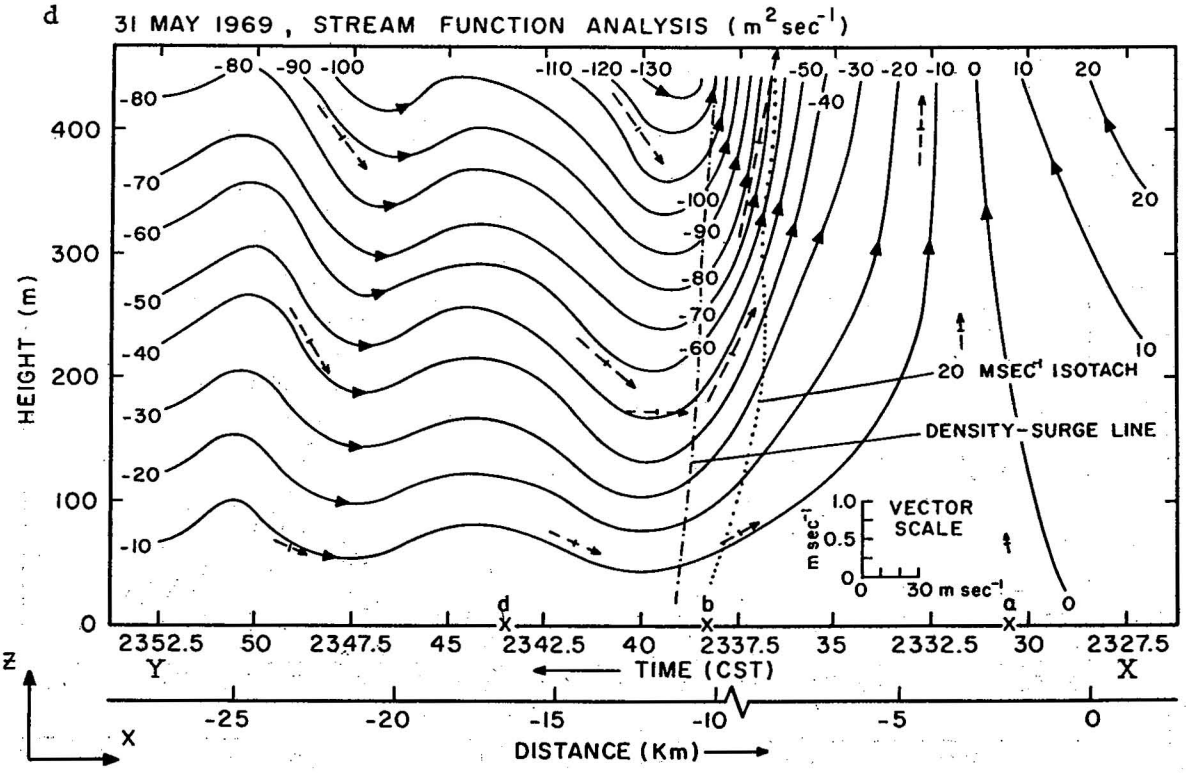

Figure 9 (Continued)

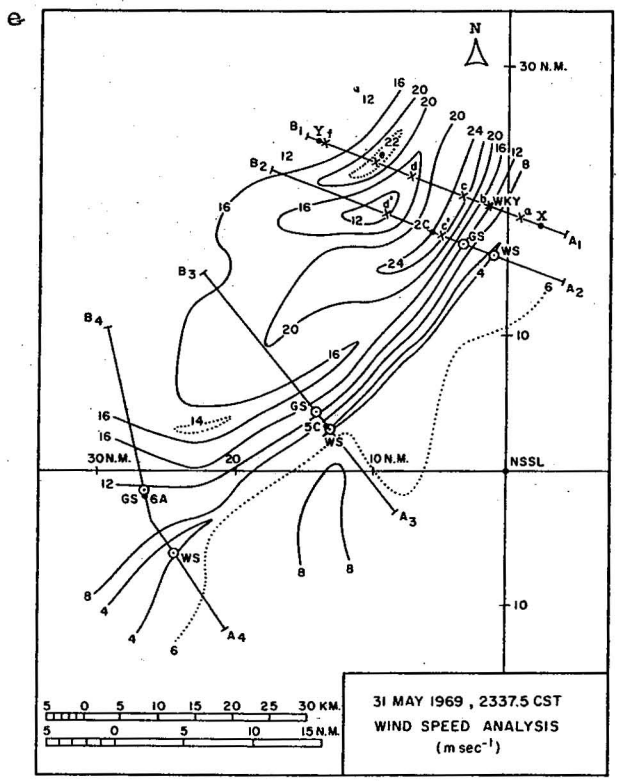

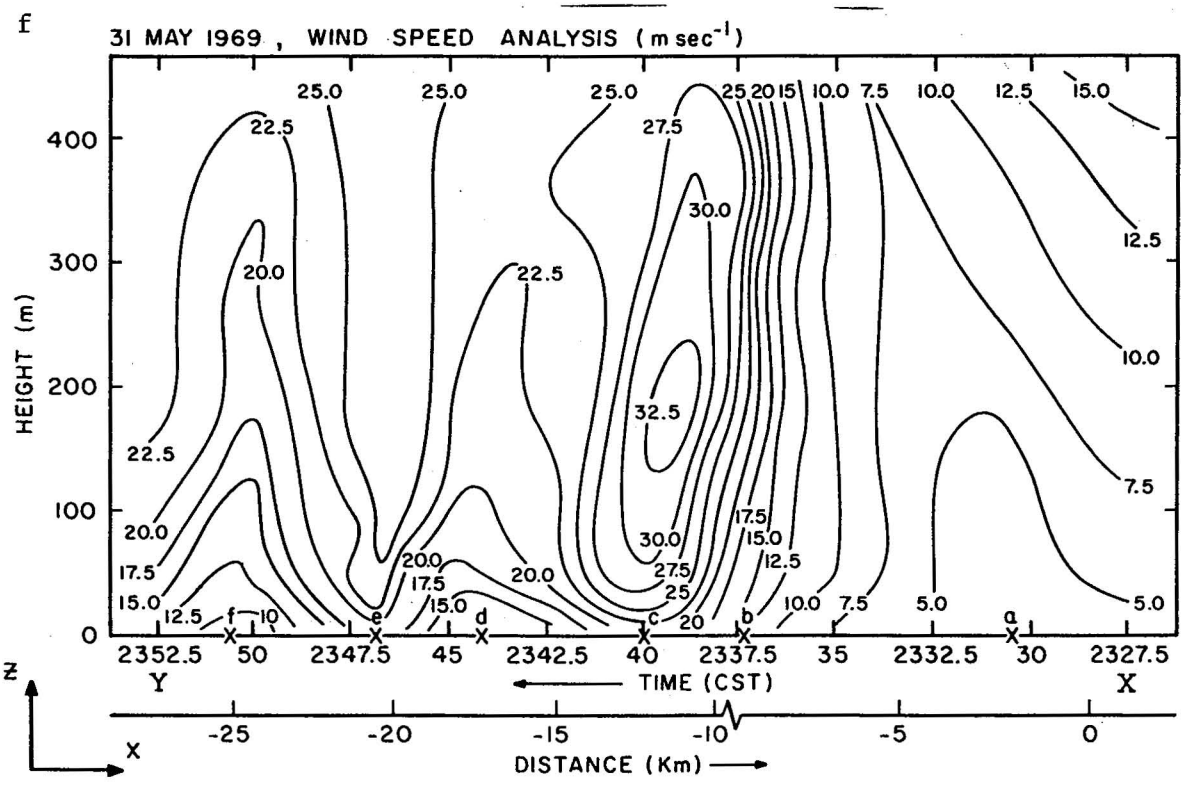

Figure 9 (Continued)

g

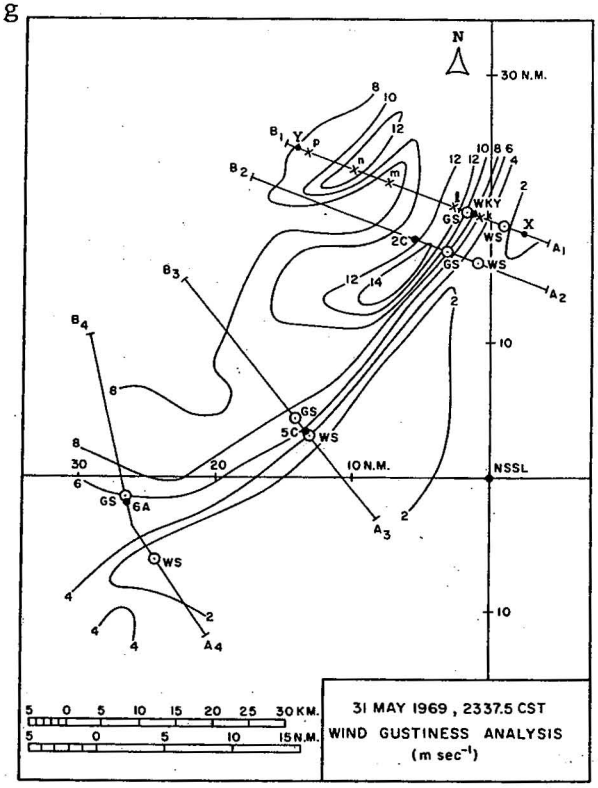

h

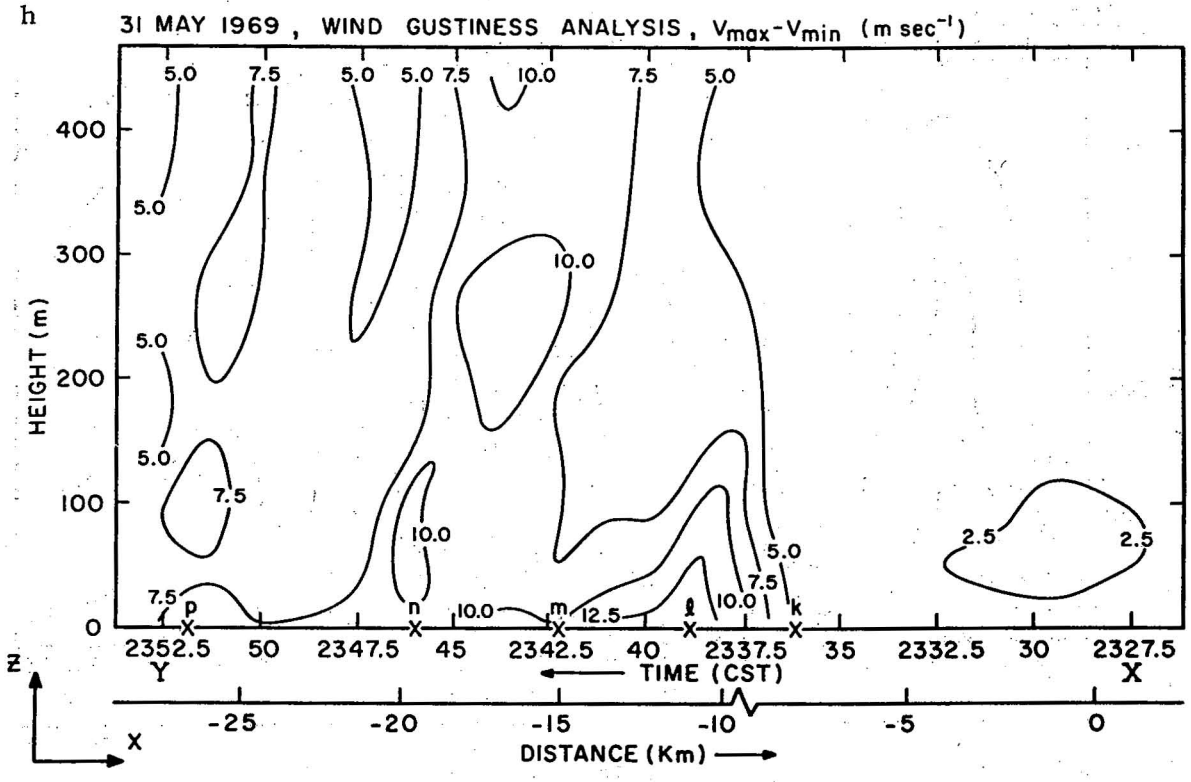

Figure 9 (Continued)

and c. The surface wind veered sharply from a uniform southerly flow to northwesterly behind the windshift line (see also figure 10). The vertical cross section (figure 9b) reveals that the windshift sloped upstream with height at an angle of only 7° above the horizontal. Figures 9e and f exhibit a distinct speed minimum coincident with the windshift at all levels. Based on the author's observations, the speed minimum seems to be a quite typical feature, corresponding to the commonly known "lull before the storm." The horizontal wind velocity divergence at the base of the windshift was about -15×10^{-4} sec^{-1} (see figure 9c) which reflects the uniform upward motion field computed to be 1 m sec^{-1} at 400 m (figure 9d).

No change in the thermodynamic air properties is evident across the windshift. The ambient temperature and wet-bulb potential temperature patterns (figure 11a and b, respectively) are virtually isothermal across this wind change line; thus, no change in air mass is indicated (also see figure 10).

The most striking change coinciding with the windshift was the sharp surface pressure rise (see figures 10 and 12). The pressure rise was quite uniform along the windshift line. The average pressure increment across the windshift was 3.5 mb, and the horizontal pressure gradient was 0.6 mb km^{-1}. This change satisfies the National Weather Service's definition of a pressure jump (PJ) (see figures 10 and 12). Immediately following the pressure rise a return to a constant level (PL) persisted until the arrival of the gust surge.

5.2.2 Gust Front

Generally, the analyses revealed the gust front as a high speed, gusty wind current of practically uniform direction and led by an intense gust surge. Depicted qualitatively by the spacing of the streamlines in figure 9c, the intensity of the gust surge and speed of the upstream current was significantly greater in the region of stations WKY and 2C than at 5C and 6A. Focusing on the analysis at WKY, figure 9a and 9b show that only minor horizontal wind veering accompanied both the gust surge (point b) and a secondary surge (point d). Wind direction changes in the vertical direction were similarly small. The isotach pattern in the X-Z plane (figure 9f) displays the gust surge as an intense wind-surge "wall" that is retarded near the ground. This frictionally induced surface retardation is evidenced by a forward gust-surge slope described by a rise of only 250 m within 2 km in the downstream direction. The horizontal speed gradient through gust-surge zone increased with height to a maximum value of 10 m sec^{-1} km^{-1} at 335 m. At the crest of the gust surge, a peak in the horizontal wind speed occurred as shown in the network isotach pattern (figure 9e). Note that the speed maximum near stations 2C and WKY was about 8 m sec^{-1} greater than at stations 5C and 6A (see also figure 10). The speed pattern in the X-Z plane (figure 9f) shows that the speed maximum occurred at the gust-surge crest at all levels. Interestingly, the level of maximum wind speed core of 33 m sec^{-1}

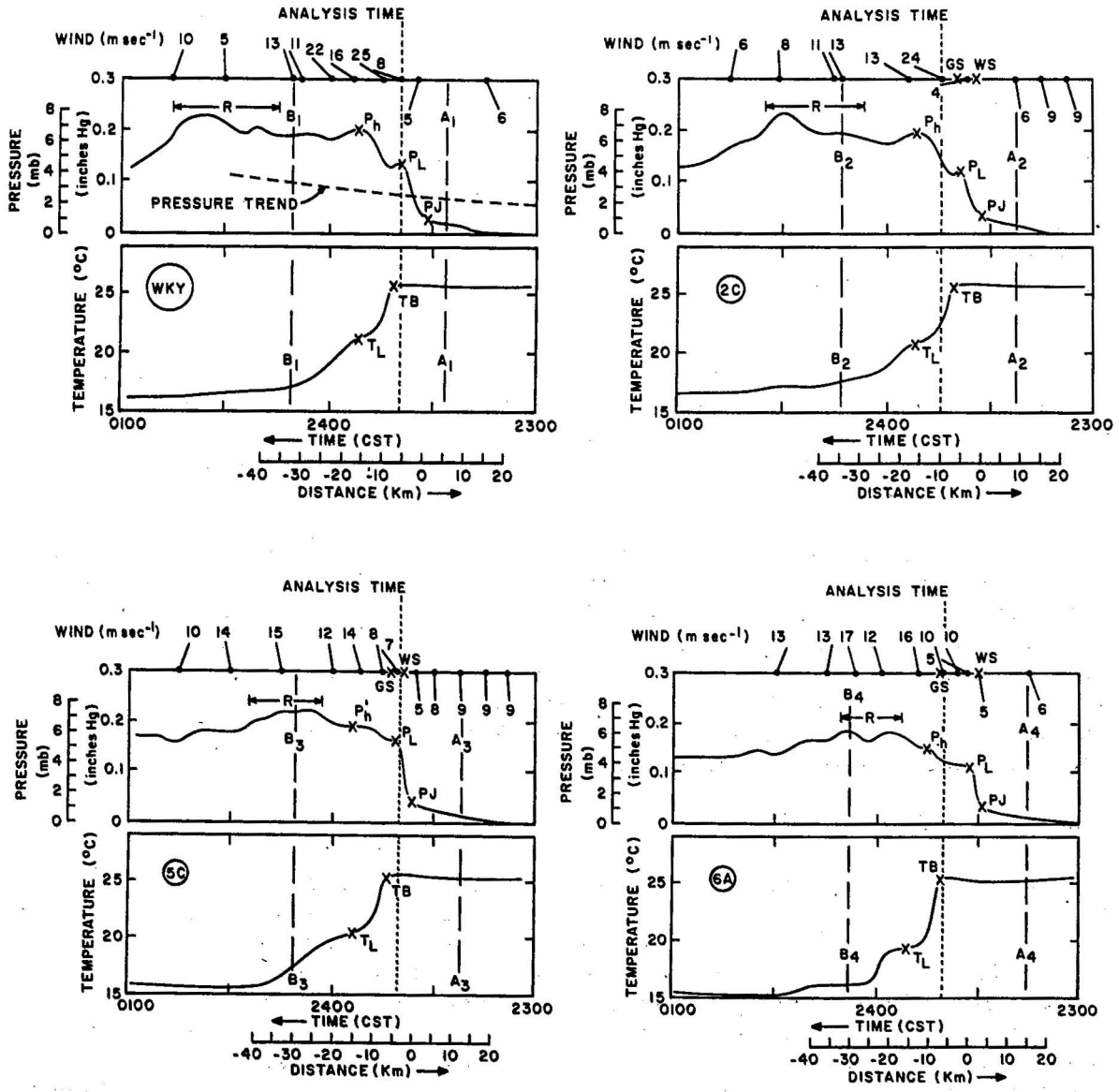

Figure 10. Spatial variations of surface wind, pressure, and temperature normal to the gust front obtained by transforming analog measurements at stations WKY, 2C, 5A, and 6A to space. The pressure trend for WKY is shown (dashed). The segments A_1B_1, A_2B_2, etc. span the surface network as shown in figures 9, 11, and 12. The significant features labeled in the wind (figure 9), temperature (figure 11), and pressure (figure 12) fields are also indicated above. The significant points in the pressure and temperature profiles are: PJ-pressure jump, P_L-temporary leveling off period in the pressure curve, P_h-pressure head (P_h', if very weak), TB-temperature break, and T_L-temporary leveling off period in temperature curve. The position of heavy surface rain is "R".

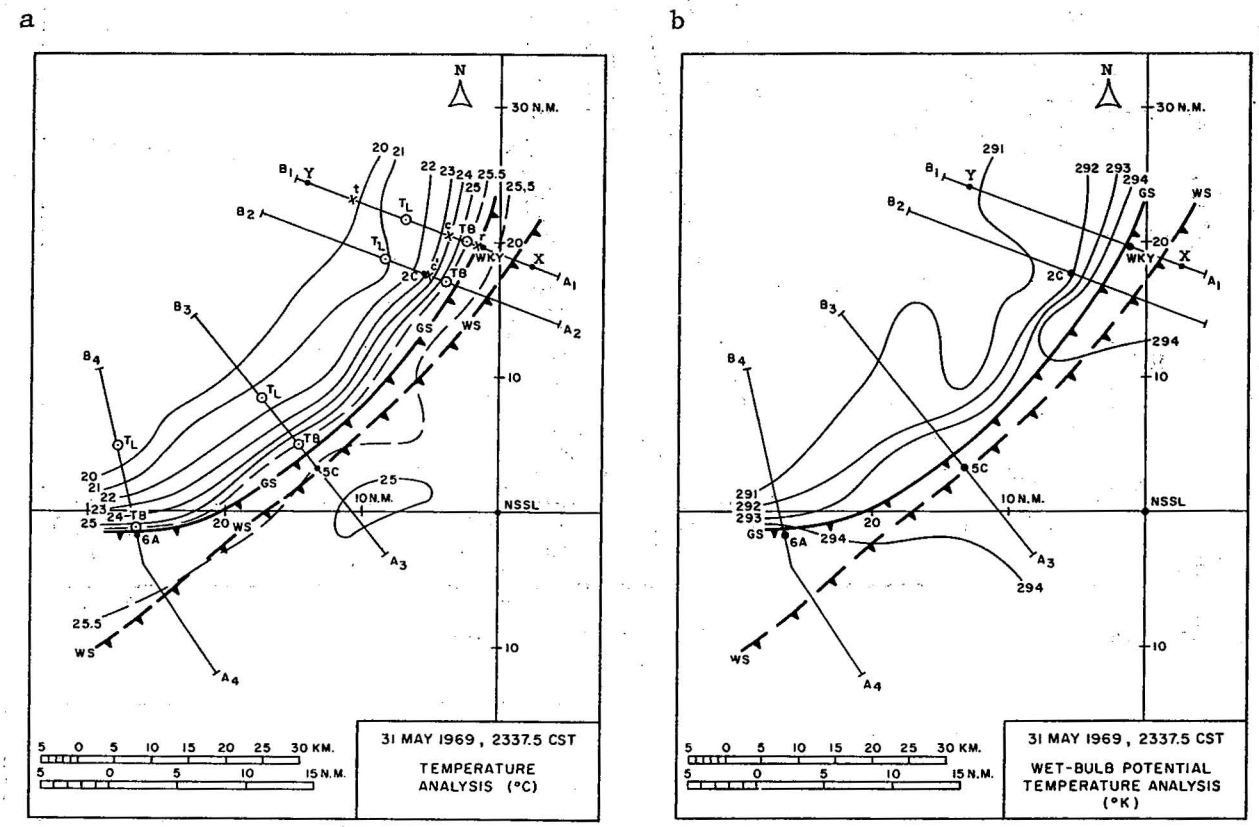

Figure 11. Network and tower temperature analyses: a) surface air temperature, b) surface wet-bulb potential temperature, and c) (next page) temperature cross section XY. Significant features are marked and labeled on the respective fields as before. See figure 10 for continuous temperature variations normal to the gust front along the cross sections indicated A_1B_1, etc.

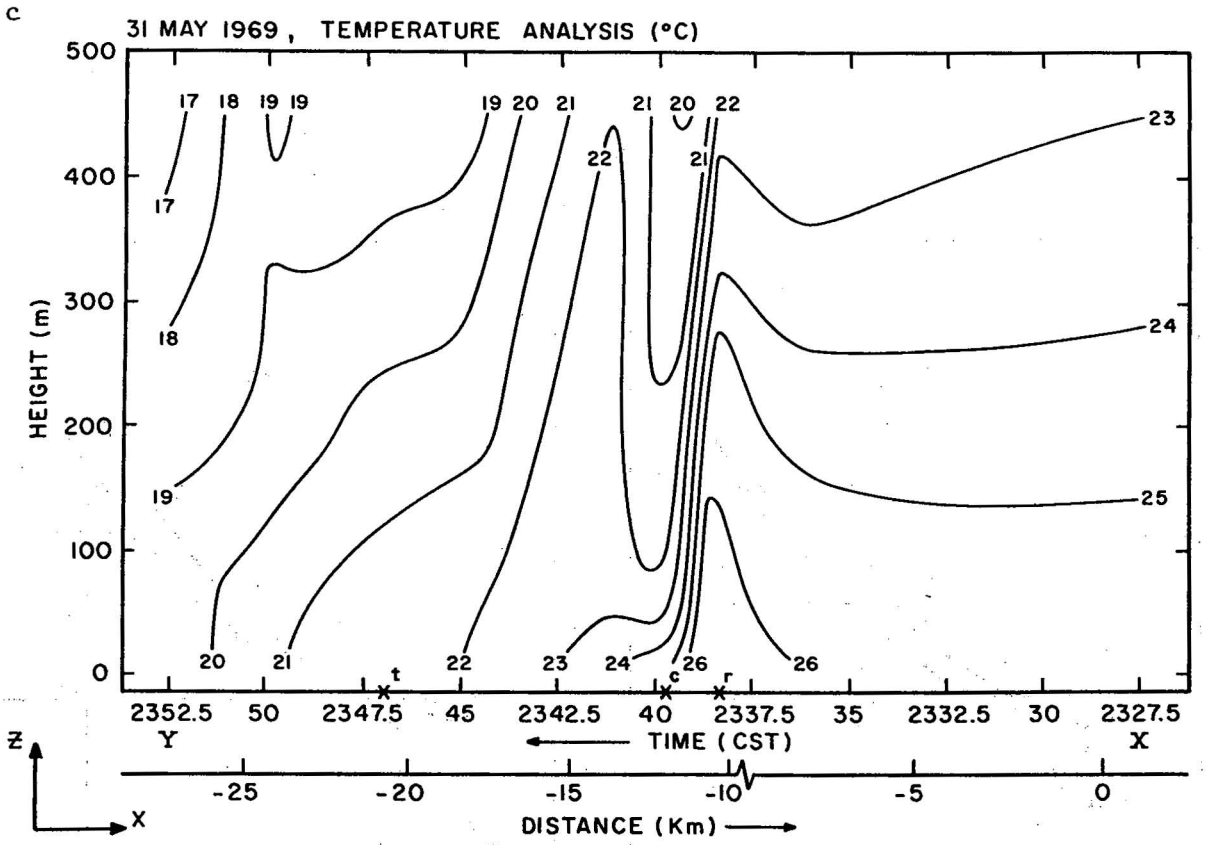

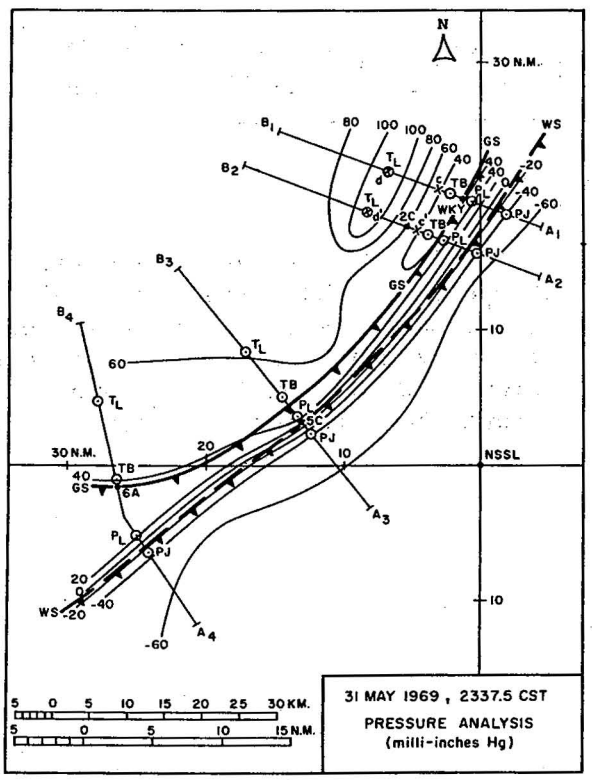

Figure 12. Surface pressure analysis. The pressure values are deviations from the large-scale pressure trend (shown for WKY in figure 10). Significant features appearing in the wind speed analysis (figures 9e and 9f), temperature analysis (figure 11), and pressure curves (figure 10) are marked and labeled identically in the pressure field.

was located only 177 m above ground. In conjunction with this low-level speed maximum, an extreme vertical wind shear of 160 m sec^{-1} km^{-1} occurred in the layer 0 to 50 m.

About 9 km upstream from the initial surge, a secondary wind surge and speed maximum occurred within the gust front. It is located by point e in figure 9e and f. The network speed pattern indicates the secondary surge had a small horizontal extent, although its definition throughout the vertical section is rather clear; thus, it apparently was a relatively small-scale secondary surge within the overall wind system.

The large surface wind convergence within the gust surge reflected the large upward motion aloft. Typical divergence values are shown to be about -25×10^{-4} sec^{-1} (figure 9c). However, on a grid much finer than the 5 km grid employed in the computation of the surface velocity divergence, a maximum surface value of -5×10^{-3} sec^{-1} is obtained. Above 250 m, the peak divergence was -1.2×10^{-2} sec^{-1} ; this value agrees with convergence values above an intense surface cold front as obtained by Browning and Harrold (1970). The stream function pattern and the inserted wind vectors (figure 9d) exhibit upward velocities as high as 2.5 m sec^{-1} within the gust-surge zone at the 400 m level. In the wake region of the maximum speed core, a broader area of weaker downward motion feature typical values of 0.8 m sec^{-1} at the same level. Upstream from the gust-surge crest, the divergence pattern was no longer uniform in the y-direction. The nonuniformity reflects the cellular pattern of the velocity field in the region of the secondary surge. In that region, the assumption inherent in the stream function calculation, i.e., $\partial u/\partial x << \partial v/\partial y$, is not valid, and the stream function pattern must be considered suspect. However, it seems safe to interpret the stream function pattern insofar as to state that the flow pattern about the secondary surge has a qualitative resemblance to that of the initial surge.

The wind gustiness at the ground is found to be proportional to the surface wind speed, but above 100 m a quite different pattern is revealed. The surface network analysis (figure 9g) illustrates that areas of maximum gustiness coincide with areas of maximum speed (figure 9e). On the other hand, figure 9h shows that above the ground relatively low values of gustiness coincide with the maximum speed core shown in figure 9f. Instead, high gustiness occurred both beneath the forward sloping maximum speed core and, upstream, in the wake of the maximum speed core in a zone of relatively low wind speeds. A similar pattern appeared in connection with the secondary surge.

Several important aspects of the gust front's thermal structure are illustrated in the analysis shown in figure 11. (1) A narrow temperature ridge (point r in figure 11c) appears at low levels just ahead of a steep fall. The magnitude of the temperature ridge is greater in the lower levels, but it disappears at ground level. The vertical temperature gradient within this ridge in the layer 100 to 444 m was superadiabatic. (2) Upstream of the thermal ridge peak a sharp

temperature fall is featured (also see figure 10). In the fall zone the horizontal temperature gradient at the ground was only 1°C km^{-1}, but aloft it was 4°C km^{-1}. The large thermal gradient also appears in the surface wet-bulb potential temperature field (figure 11b). (3) Just upstream of the temperature fall zone, a minimum temperature axis appears but only above ground level (point c in figure 11). The minimum temperature core coincides with the maximum speed axis below 100 m but lags behind it by 1 km at higher levels. (4) Upstream of the cold core is a broader zone of warmer air coinciding with the downward motion region appearing in the stream function field (figure 9d). This thermal ridge, exhibiting a magnitude of almost 2° at the tower top, appears as only an isothermal region in the surface network analysis (point T_L in figures 10 and 11a). (5) And finally, in connection with the secondary surge (point 5) a rather ill-defined thermal pattern is illustrated; however, the thermal structure near the 400 m level of the tower bears some resemblance to the thermal pattern of the initial cold surge.

Over the network the surface pressure surge connected with the gust surge was proportional to the latter's intensity (figures 10 and 12). Between stations 5C and 6A, the pressure rise following the gust surge was only about 20 milli-inches Hg (0.7 mb). At the same time, the pressure rise in the region of 2C and WKY was quite steep and the total was in excess of 60 milli-inches Hg (2 mb). The "pressure head" (denoted P_h in figure 10) was centered in the isothermal zone (T_L in figure 12) following the sharp temperature fall at the surface. Immediately upstream from the pressure head, the pressure field becomes invariant at the elevated value and remains so up to the position of the heavy rain gushes (labeled R in figure 10).

The analytical features in all the vertical cross sections at WKY are combined in the schematic model shown in figure 13. The surface pressure trace at WKY is also shown.

6. APPLICATION OF THEORIES AND MODELS TO THE ANALYSIS

6.1 Relationship of Windshift to Gust Front

Recall from the previous chapter that the leading edge of the cold outflow in the layer below 444 m was preceded by a sharp surface pressure jump that coincided with a windshift. In view of the objective of constructing a complete structural picture of the 31 May gust front, it is necessary to determine if the windshift and pressure jump were an integral part of the gust front, or if they were only somehow indirectly related to it. We inititally proceed towards this determination by considering two hypothetical cases. Case X depicts a physical situation in which the cold outflow current was mechanically pushing warm air horizontally ahead of it causing a low-level "back-current" (see Fujita, 1963, figure 28) in that region. The forward edge of the backcurrent would correspond to the windshift. In case Y, the windshift is hypothesized to be the remnants of a once strong gust surge but since

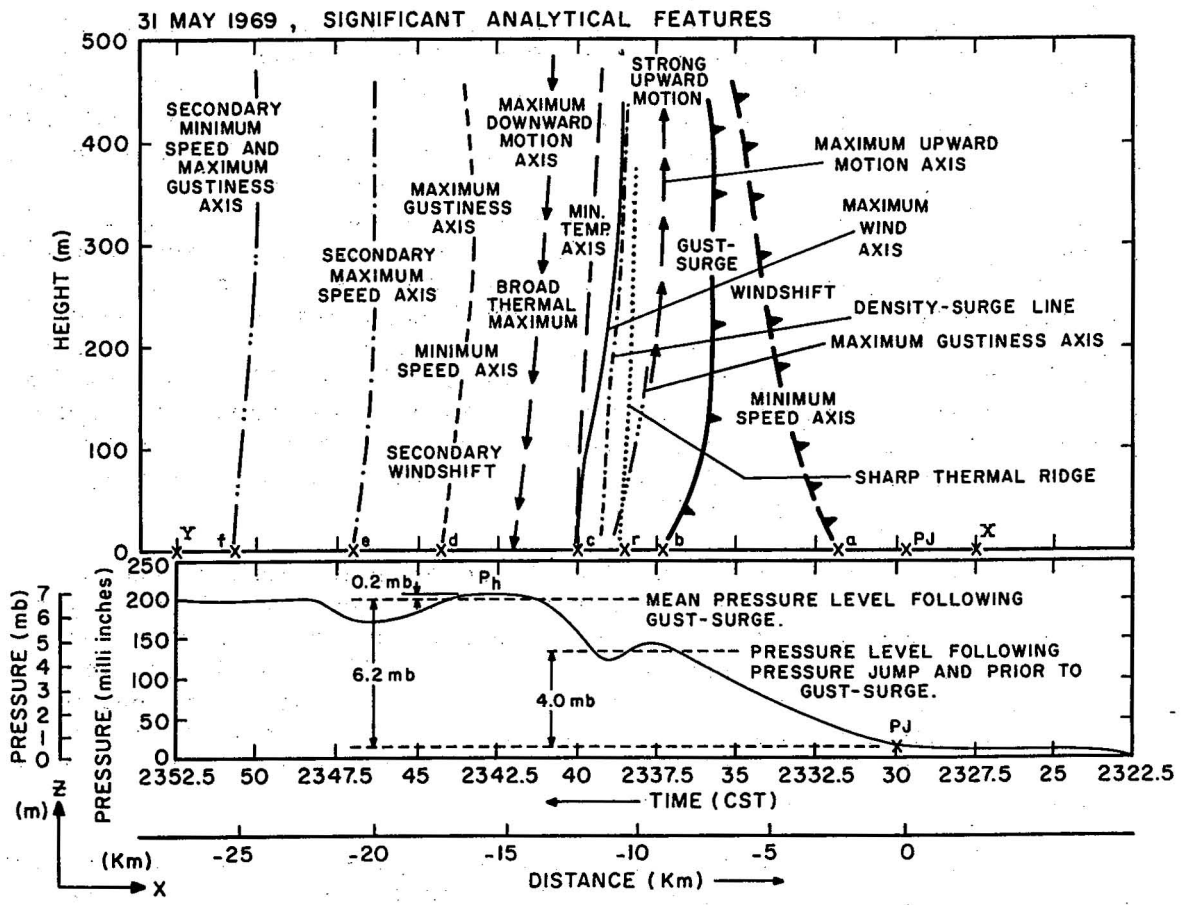

Figure 13. Schematic of the important analytical features of the wind and thermal structure of the windshift and gust front at WKY (upper). The surface pressure profile at WKY is also shown (lower).

diffused by turbulent mixing. In this case the windshift would be considered part of the outflow air mass, whereas in case X it is related but not considered an integral part of it. Now, comparing the structural characteristics of the windshift with the imagined properties of the hypothetical cases to check for physical inconsistencies, case X is inconsistent with these analytical features: (1) the windshift and gust surge were not parallel, (2) the latter propagated 6 m sec^{-1} faster than the former and (3) most decisively, a large uniform pressure rise existed across the windshift. Case Y is in disaccord with the (1) observed sharp pressure gradient coincident with the windshift and (2) more important, observed lack of any evidence of a density change across the windshift line. These inconsistencies rule out the applicability of either of these two mechanisms to explain the initial pressure- and wind-change lines.

Other documented case studies of severe squall lines (Tepper, 1950; Fujita, 1959) have revealed leading discontinuities that were partly or totally independent of changes directly related to the squall line. From his investigation of the squall line of 16 May 1948 over the Ohio cloud physics network, Tepper (1950) found that a surface pressure jump led all other surface weather changes. On the basis of the time sequence and nature of the surface parameter changes following the pressure jump, he concluded that "the pressure jump is independent of other parameters, and that the behavior of the pressure profile can be explained only in part by the temperature break, wind shift, and/or rain gush." Fujita's (1959) mesoanalysis of the severe local storms, Kansas-Oklahoma network data of the 25 June 1953 squall line showed a pressure jump- and windshift line more than 50 miles ahead of a second pressure-surge line accompanied by vigorous thunderstorm activity. Fujita postulated the leading pressure-jump line was not directly coupled with the one that followed.

The nature of the leading windshift and pressure jump of the 31 May 1969 squall line is similar to that found by Tepper (1950) and Fujita (1959), in that the surface pressure and wind changes could not be attributed to changes occurring upstream. Recall from figure 11c that no significant density changes occurred across the windshift below 444 m. The density surge associated with the gust front at WKY was 10 km upwind of the windshift; in addition, the precipitation echo (at 11 heights) was much further upstream.

Thus, the analysis shows that the surface pressure-jump and windshift lines were practically coincident but lacked a density change across them, throughout the period of their translation over the network. Further deductive reasoning leads to the suggestion that the windshift was a manifestation of horizontal accelerations of air parcels in response to the passing pressure gradient. The practically undisturbed thermal field of air below 444 m implies that the atmospheric phenomenon causing the pressure disturbance was substantially above the tower summit. The following section considers a possible mechanism of such a disturbance.

6.2 Gravitational Wave Model Applied to Windshift

Following his studies on the nature of pressure-jump lines through mesoscale and dynamic analysis, Tepper (1950) proposed a mechanism of the pressure jump as an analogy to the hydraulic jump in liquids. According to his theory, the initial stage of a pressure jump occurs when a sudden forward acceleration of a cold front acts as a piston to elevate a low-level temperature inversion in the warm air ahead of the front as a gravitational wave. The propagating temperature inversion wave gradually develops a very steep slope on its forward side. Tepper drew an analogy between this atmospheric density-interface jump and the hydraulic jump which can propagate on the interface of stratified fluids of different densities. In the atmosphere the sharp

surface pressure rise is a reflection of the passage of the inversion jump aloft. Thus, he called the surface manifestation a pressure jump. He further postulated that the pressure jump is an effective mechanism for the development and maintenance of the pre-frontal squall line.

An investigation of the evolution of the 31 May 1969 squall line yielded substantial evidence of the applicability of such a mechanism. It was found that (1) rawinsondes at Amarillo, Texas (AMA), Dodge City, Kansas (DDC), and TIK revealed thermal inversions near the 750-mb level exceeding the 5°C potential temperature increment at the interface which Tepper specified to be sufficient for gravity-wave maintenance. (2) As illustrated in figure 3 a sudden frontal acceleration occurred in Colorado and Kansas during the afternoon of 31 May 1 to 2 hr before thunderstorm development in the southern extremities of those states. (3) Pressure jumps were reported ahead of the front from AMA to Tulsa, Oklahoma (TUL), and about 10 n miles ahead of the heavy precipitation echoes of the squall line at Hobart (HBR), OKC, and Ponca City (PNC) (note PJ's in figures 3, 4b, 4c, and 4f).

Five years later, Tepper (1955) developed a simple pressure-jump model whereby the equations of motion and mass continuity for frictionless, incompressible flow were applied to a two-layer, hydrostatic atmospheric model. Each layer was homogeneous in density, and the density of the lower layer was greater than that of the upper layer. The lower layer was initially injected with a narrow, high-momentum air-current impulse oriented in a north-south direction. Graphical integration of the governing equations revealed that within 2 hr of the initial perturbation a density interface jump, accompanied with an eastward component of air motion, was propagating eastward from the axis of the initial current.[6] At the same time, an interface depression was traveling west from the identical origin. After about 6 to 8 hr, the eastward propagating gravity wave had undergone dramatic steepening of the slope of the interface and sharp intensification of the eastward flow speed across the jump zone (Tepper, 1955, figures 9 and 11). In an atmospheric application, Tepper found that the steepened gravity wave appearing in his model could also develop and propagate on naturally occurring atmospheric thermal inversions; the surface manifestation of such an inversion jump is a pressure jump and an associated windshift.

Tepper's (1955) model was applied to the ambient atmosphere over the network on the evening of 31 May. First consider the thermal and density profiles shown in figures 14a and 15, representing conditions just before the onset of the squall line. These profiles were obtained from the 1800 CST 31 May 1969 TIK sounding, modified in the lower 444 m by substituting the surface pressure and tower temperatures at WKY

[6]Presumably, an initial perturbation caused by an abrupt frontal acceleration would also initiate such a traveling wave.

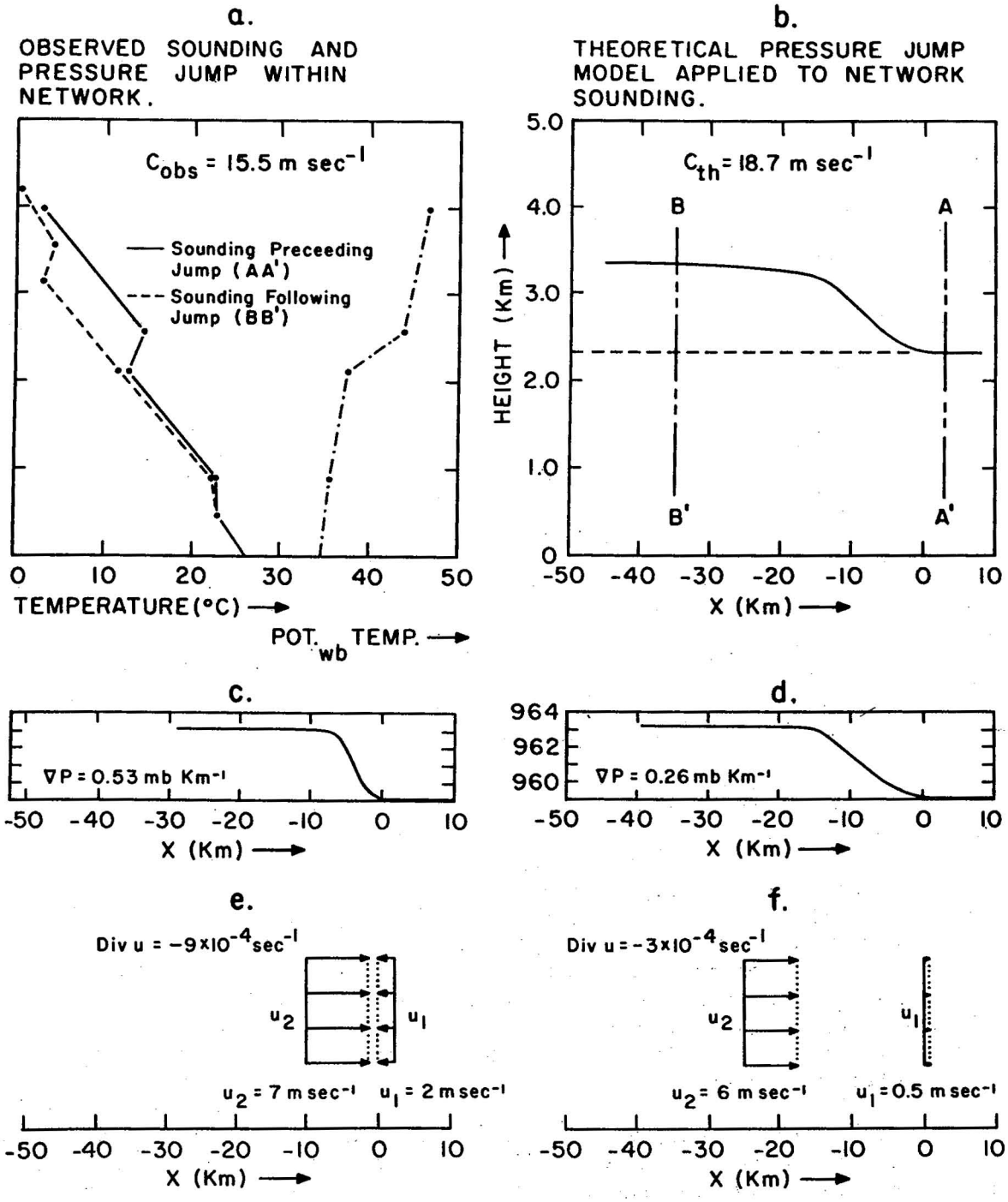

Figure 14. Comparison of the observed and theoretical pressure jump of 31 May 1969. (a) Ambient and wet-bulb potential temperature profiles obtained from the 1800 CST TIK rawinsonde, modified in the lowest 500 m for the WKY tower conditions at 2300 CST. (b) Profile of the thermal inversion through the gravitational wave "jump" as obtained by application of Tepper's (1955) pressure jump model to the thermal inversion shown in (a). (c) Typical surface pressure profile through the observed pressure jump. (d) Computed hydrostatic pressure profile at the surface beneath the gravitational wave in (b). Windshift across the observed (e) and theoretical (f) pressure jump.

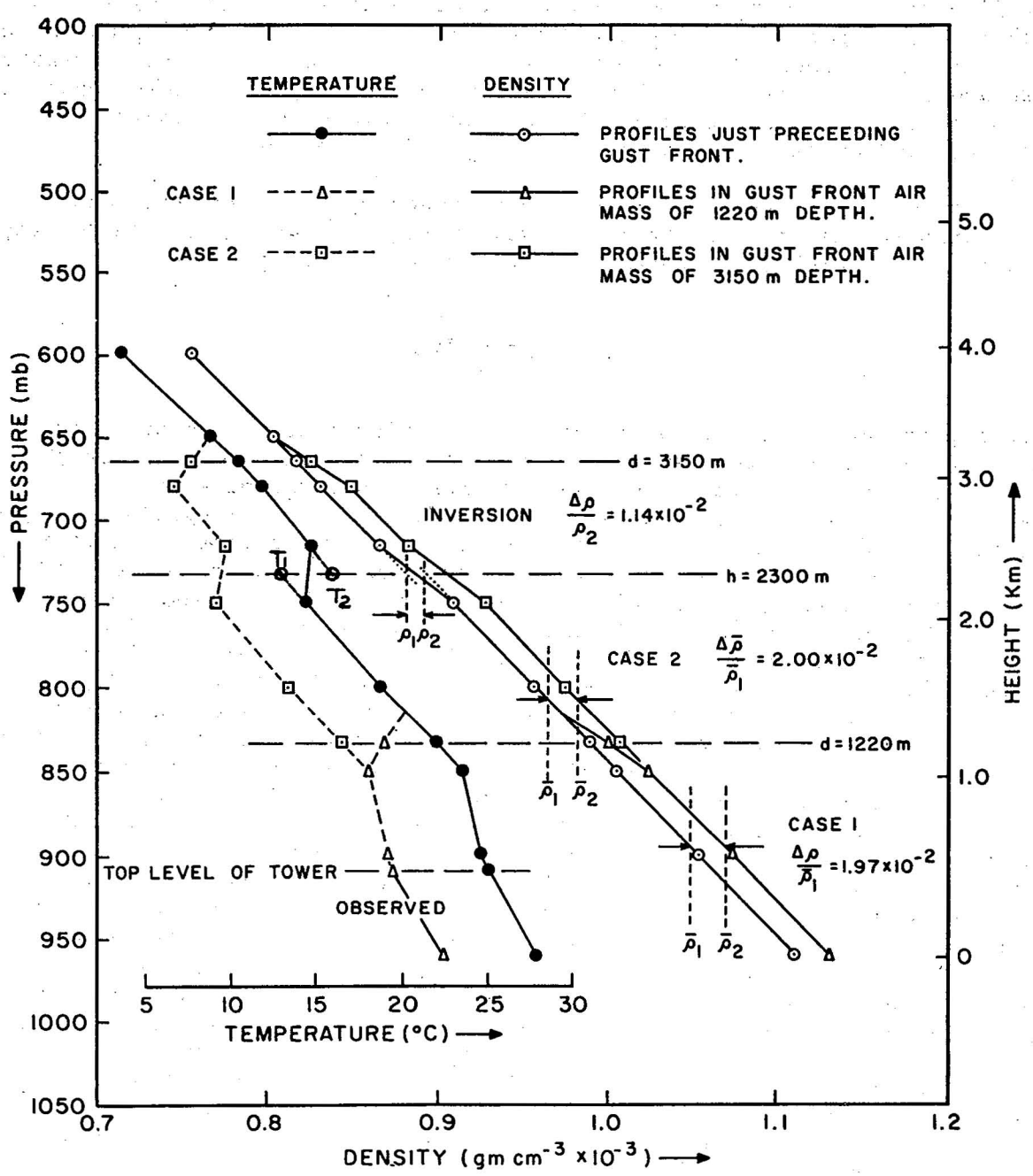

Figure 15. Vertical profiles of temperature and density at WKY just before and just after the gust surge passed, 2300 and 2345 CST, respectively.

at 2300 CST. The slight temperature inversion at 2300 m (figure 15, inset) had a density ratio, $\rho_2 - \rho_1 / \rho_1$ (or $\Delta\rho / \rho_1$) of 1.14×10^{-2}, where ρ_1 and ρ_2 are the respective air-parcel densities above and below the inversion layer extrapolated linearly to 2300 m, as shown in figure 15. In this sense ρ_1 and ρ_2 represent the densities of air parcels specified by the ambient pressure and hypothetical temperatures T_1 and T_2 at 2300 m.

Following Tepper's model, the phase speed c_o, of a gravitational wave jump in the initial stage of development, propagating on the density interface of height, h, separating the two layers, is given by

$$c_o = \sqrt{\frac{\Delta\rho}{\rho_1} gh}, \tag{5}$$

where g is the gravitational constant. Assuming that the density interface in the atmosphere over the network on 31 May could be taken as the 2.3 km thermal inversion, and inserting its associated numerical parameters into (5) yields a c_o value of 17.7 m sec^{-1}. Tepper's numerical results (figure 8, in his article) specify that by the time the wave is fully developed the phase speed of its crest is 1.15 c_o or 20.2 m sec^{-1}.[7] These values correspond closely to the network-average propagational speed of the windshift and pressure jump, observed as 15.5 m sec^{-1}. The shape of the thermal inversion profile within the gravitational wave jump, as obtained by application of Tepper's numerical results to the 31 May atmosphere, is sketched in figure 14b. The inversion is elevated about 1 km at the crest of the wave. As the jump propagates along the interface, ambient air parcels are displaced upward, undergoing adiabatic cooling as they ascend, which results in a new temperature profile as shown by the dashed line in figure 14a. The temperature profile was obtained by lifting air parcels on a thermodynamic chart 1 km at the thermal inversion; the amount of lifting of air parcels above and below the inversion was decreased linearly to zero at a vertical distance of 1.5 km away from the inversion. The plot of the computed surface hydrostatic pressure increase due to the cooling is shown in figure 14d. A comparison of the network-averaged pressure profile in the jump zone with the computed pressure profile below the interface jump shows almost identical magnitudes of the total pressure change; however, the observed pressure gradient is almost twice as large as the theoretical value. Similar correspondence is seen in the observed and theoretical wind regimes (figures 14e and f, respectively). The wind pattern within the theoretical jump was obtained directly from figure 8 of Tepper's (1955) article, while the observed windshift pattern represents the result obtained by averaging the measured wind speed components in the vertical plane normal to the windshift. Just as for the pressure, the magnitudes of the observed and theoretical wind change across the jump are remarkably similar, but the former has a larger gradient than the latter.

[7] This result assumes an atmospheric Froude number, F_o, of the initial perturbation equal to 1.

Summarizing, evidence has been shown to demonstrate that atmospheric conditions, allowing the applicability of Tepper's theory of gravity wave formation and propagation on a thermal inversion in connection with squall line development, were present on 31 May 1969. Synoptic station reports pressure jumps occurring ahead of the cold front and at the leading edge of the squall line suggest that a gravitational-wave jump was associated with these features. The application of numerical results from Tepper's dynamic pressure jump model to the ambient atmosphere over the network yielded a gravity-wave jump whose associated phase speed, surface pressure pattern, and windshift were remarkably similar to corresponding changes accompanying the observed pressure jump and windshift.

The above deductions give reasonable evidence of the validity of the gravity wave hypothesis to explain the observed pressure jump and windshift ahead of the gust front; however, a conclusive statement about this cannot be made, because verifying observations and/or measurements were not made.[8] Even if such a theory could be adequately verified the question regarding the coupling to the gust front to the gravity wave would still remain to be answered. On the other hand, an adequate basis has been established to conclude that the pressure and wind changes ahead of the gust surge were not inherent structural features of the outflow air mass of the precipitation echoes. This is actually the only conclusion relevant to the examination of the gust front structure.

6.3 Gravity Current Model Applied to Gust Front

A gravity current (often called a density current) when involving liquids is a stream of high density fluid along the horizontal bottom and displacing an ambient fluid of lesser density. The motive force is a horizontal pressure gradient across the lateral interface separating the two fluids; this arises because of the relatively larger hydrostatic pressure within the heavy fluid (Benjamin, 1968). In the steady phase of gravity flows, a dynamic balance exists between shear stresses and the pressure gradient force. Among common examples of gravity currents in nature is one that occurs when a body of saline water intrudes into a fresh water estuary, or when a mass of muddy water displaces clear water along the bottom of a reservoir ("turbidity" current), a phenomenon often noted even by the casual observer. An excellent photograph of a gravity current produced in a laboratory is seen in figure 16a (taken from Simpson, 1969). The white fluid mass is a saline water solution of specific gravity of 1.01 and is surging to the left along the bottom of a long trough filled with pure water.

---

[8] Colmer (1971) and this author as well have observed that a windshift, often accompanied by a sharp pressure surge, is a frequent feature preceding the initial surge of the cold outflow of thunderstorms. This problem remains and deserves further examination.

a

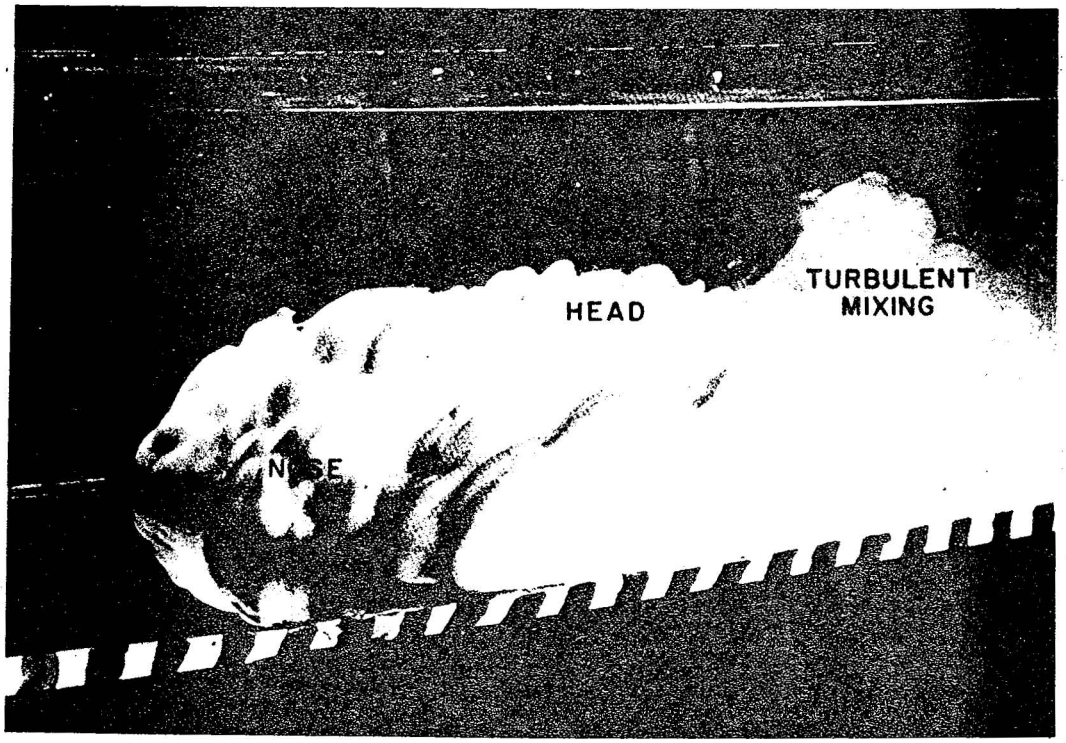

b

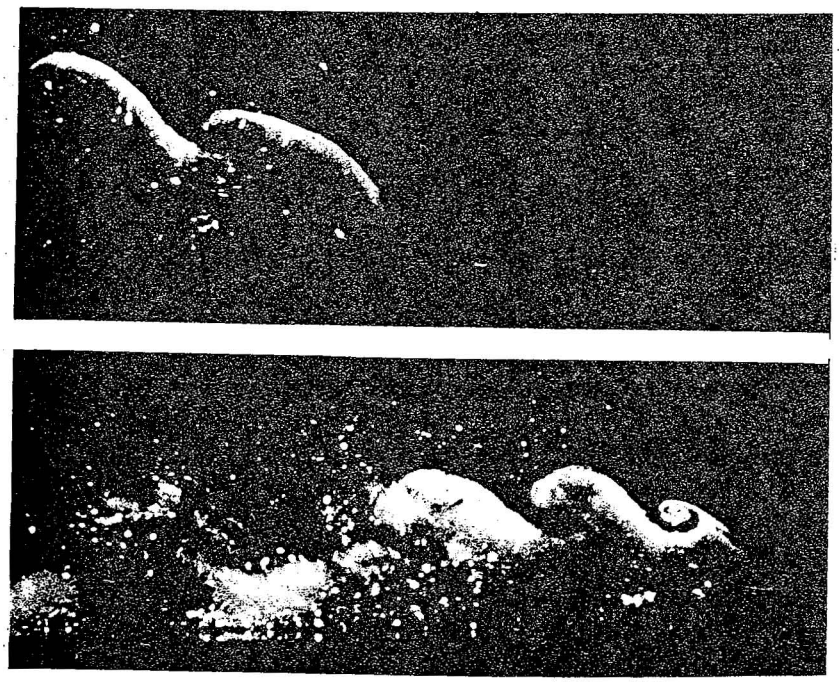

Figure 16. (a) A saline "density current" (gravity current) propagating from right to left along the bottom of a transparent tank filled with pure water. Note the slightly elevated head and the turbulent mixing in its wake. (b) A saline current (flowing from left to right) revealing the formation of bulges which are swept backwards and roll up in the form of billows and then break up (after Simpson, 1969).

Gravity currents in the atmosphere are less obvious because of the complexities of atmospheric flows introduced by horizontal and vertical inhomogeneities of air density, compressibility effects, flow over irregular terrain, and the effects of the earth's rotation. Then, there is the added problem that atmospheric gravity currents are usually invisible, because they are normally devoid of condensation. However, in some cases dust is picked up by strong surface winds and carried to great heights, i.e., 1 to 2 km, near the front of such cold surges making the "nose" of the currents clearly visible. Two examples are illustrated in figure 17. Figure 17a is a large-scale cold front in Kansas, and figure 17b is a "downdraft haboob," the name given to the cold outflow of thunderstorms carrying high wind gusts and suspended sand, in Sudan. Berson (1958), Clarke (1961), and Simpson (1969) have shown that such atmospheric flows have similarities to gravity currents, i.e., as defined at the beginning of this section and as revealed in laboratory experiments. Clarke (1961) and Simpson (1969) have shown that sea-breeze flows having a duration of less than a day also display some structural and displacement characteristics common to gravity currents.[9] This portion of this study examines the gust front for structural and displacement features that characterize gravity currents.

The nature of gravity currents has been investigated theoretically as well as in laboratory and numerical simulation experiments. Von Karman (1940) introduced a simple theoretical model of a "perfect-fluid" gravity current propagating steadily along the horizontal bottom of an infinitely deep tank of relatively less dense fluid. The infinite depth of the environmental fluid allowed him to assume that the latter is undisturbed relative to the propagating heavy fluid; the perfect fluid assumption implies that the flow is energy conserving. Using a coordinate system translating along with the gravity current of speed, V, he applied Bernoulli's equation for steady, incompressible, irrotational flow to points A and B along the streamline on the interface separating the gravity current and the ambient fluid (see figure 18). This equation applied to the upper fluid of density, ρ_1 (assuming A is a point of stagnation), gives

$$P_A = P_B + g\rho_1 d + \tfrac{1}{2}\rho_1 V^2 \quad .$$

[9] Air-mass currents having a lifetime of a day or more tend towards geostrophic balance. In this regard the relatively long lifetime of typical large-scale cold fronts, i.e., sometimes many days, would tend to rule out the applicability of gravity-current motion. However, the large horizontal and vertical wind shears found at the leading edge of large-scale cold fronts result in shear stresses that exert a much greater control over the motion than that control due to the Coriolis effect; thus, gravity-current motion occurs at the leading edge of cold fronts (Clarke, 1961). This aspect is further considered in a later section.

a

b

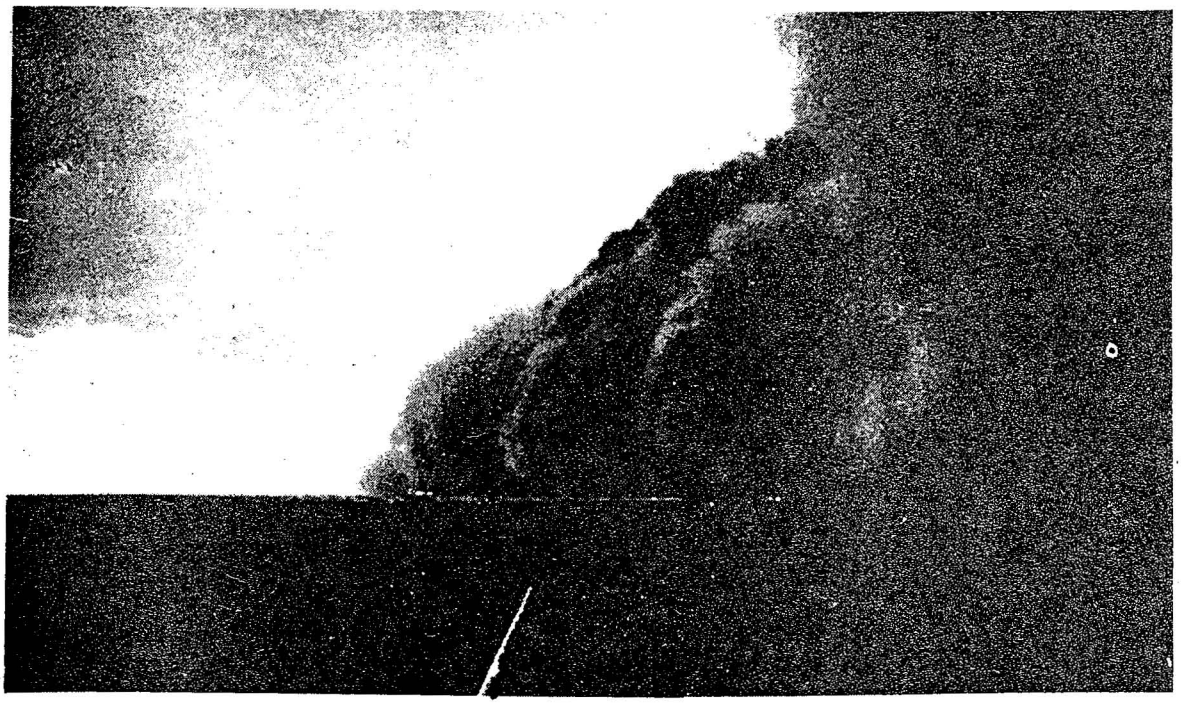

Figure 17. Atmospheric gravity currents. (a) Cold front in Kansas (courtesy of Yih, 1969). (b) Haboob in Sudan (courtesy of Simpson, 1969). The Haboob is usually found just ahead of an active or dissipating squall line, but a few cases have revealed it to be associated with a strong dry cold front. In both (a) and (b) the front is moving from right to left.

The same equation applied to the heavy fluid of density, ρ_2, and mean depth, d (realizing that the gravity current is stationary relative to the assumed coordinate system), gives

$$P_A = P_B + g\rho_2 d,$$

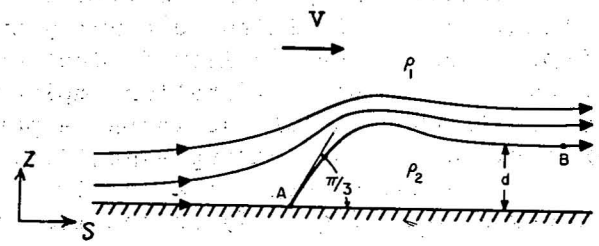

Figure 18. Schematic flow model of a gravity current of density ρ_2 at the bottom of an infinitely deep reservoir of less dense fluid. Viewed with respect to a coordinate system attached to the gravity current, moving to the left with speed V, the dense mass is stationart while the environmental flow is toward the right at speed V.

where P is the ambient pressure, and g is the gravitational constant. Combining the above two equations yields

$$V = \sqrt{2gd\left(\frac{\rho_2 - \rho_1}{\rho_1}\right)} \quad . \quad (6)$$

Gravity currents have previously been produced in laboratory tank experiments by Keulegan (1958), Middleton (1966) and Simpson (1969) (a photograph of such a fluid flow, discussed earlier, is shown in figure 16a) as well as in numerical experiments conducted by Daly and Pracht (1968). The experiments have demonstrated that greatest changes in the structure and displacement occur in the early stages of the flow, i.e., immediately following the removal of the lateral partition confining the high density fluid. Following the transient stage, the current quickly assumes a quasi-steady geometric shape and densimetric structure. This is confirmed by the near-steady displacement over the extent of the trek along the trough. During this steady stage, the displacement obeys the relation

$$V = k\sqrt{gd\left(\frac{\rho_2 - \rho_1}{\rho_1}\right)} \quad (7)$$

where the symbols are the same as before. From the numerous experiments conducted by Keulegan (1958), involving an assortment of trough geometries, and for fluid density ratios typical for alleged atmospheric gravity currents, i.e., $0.01 \leq \rho_2 - \rho_1/\rho_1 \leq 0.02$, k was found to have an average value of 1.1. The corresponding theoretical value of k implied by (6), as deduced from a frictionless flow model, is 1.414. Benjamin (1968) obtained a theoretical value of 1.23 for a model gravity current in a reservoir of finite depth where dissipative energy losses at the front of the current are taken into account (see Lamb, 1932, p. 280). This summary of documented results demonstrates reasonable consistency in findings from independent investigations and thus gives assurance of the validity of (6) and (7) to describe gravity current motion.

Because the present examination of the gust front is focused on its structural similarities to gravity currents, the boundary of the gust front must now be considered identical to the boundary of the constituent cold air. This consideration implies that the leading edge of the gust front is the zone of the sharp temperature drop. Thus, the previous definition of the leading edge, i.e., the gust-surge line, is discarded and the density-surge line in figure 13 (identical to the temperature-break line in figure 7) is assumed to be the forward air-mass boundary.

The initial step in examining the 31 May gust front for behavior as a gravity current is to apply (6) and (7) to its analytical structure and to compare the theoretical result with analytical findings. In the proper application of these equations, V is the displacement speed of the gust front relative to the flow of the ambient troposphere or, vice versa, the ambient flow relative to a coordinate system attached to the gust front. Later, it is shown that the outflow air mass had a maximum height of about 1700 m above the ground. Therefore, it seems reasonable to assume that the tropospheric flow above about 3400 m did not influence the propagation of the gust front. The mean wind vector in the surface-to-3400 m layer, revealed by the 1800 CST TIK rawinsonde, was directed almost parallel to the y-direction in figure 9c; the component in the x-direction was only +1 m sec^{-1}. Since the propagation speed of the gust front near WKY was 21 m sec^{-1} in the positive x-direction, the x-component of ambient-air flow, u, is directed toward the gust front at 20 m sec^{-1}, as seen by a coordinate axis attached to the gust front. Figures 9b and 9f also show that in the warm air ahead of the gust front below 444 m, the layer-mean of the y-component of wind speed, v, varies less than 4 m sec^{-1} along the x-direction. Assuming that the latter result is general throughout the ambient-air layer below 3400 m, then the v-component can be ignored in the derivation of the displacement speed, V, without significant error since $u^2 \gg v^2$. Thus, in figure 18, $V \approx u$ (= 20 m sec^{-1}) and the s-coordinate corresponds to the (-x)-coordinate in figure 9c.

The application of (6) and (7) further requires that the mean depth $\overline{d}$, of the gust front's associated cold air and the density ratio, $\overline{\rho_2} - \overline{\rho_1} / \rho_1$, be determined. (The bars over the density symbols denote mean values of the respective cold and ambient-air densities in the atmospheric layer accommodating the gust front.) The atmospheric measurements available for this analysis do not supply this information directly because they do not extend to the height of the cold-air dome. In fact, the vertical thermal cross section (figure 11c) implies that the gust front was far higher than the top level of the tower. According to Byers and Braham (1949) and Fujita (1963), the horizontal temperature difference between environment air and the cold outflow near its upper boundary is quite small. Figure 11c shows that the temperature drop at 444 m is almost as large as that exhibited at lower levels. Furthermore, the surface pressure rise following the cold surge was far greater than that which could be attributed to a layer of cold air less than 500 m thick.

The depth of the cold air was inferred by extrapolating the horizontal environment-to-gust front temperature decrease to a height above the tower such that the computed hydrostatic pressure at the ground matches the observed value. Since the mean depth d is desired, the mean surface pressure rise and the temperature upstream from the density surge were employed. The mean pressure increment following the gust surge at WKY is shown as 2.2 mb in figure 13. Warm-to-cold air temperature decreases of 4°C and 5°C were obtained from figure 11c, the first value representing the average fall from undisturbed environment and the second corresponding to the fall from the narrow thermal ridge just ahead of the density surge (see figure 11c). To arrive at the gust-front temperature profile above the tower, these temperature drop values were subtracted from the modified TIK sounding as illustrated in figure 15 and table 3. The cold-air depth required to account for the total pressure rise, combining rises occurring during windshift and gust surge (shown as 6.2 mb in figure 13), was also computed according to the procedure described above (CASE II in figure 15 and table 3). This depth value is to be used for a consideration discussed later.

Table 3. Parameter values for calculation of theoretical gust front speed.

		Depth	Density Ratio	Displacement Speed ($m\ sec^{-1}$)		
	Temperature Deficit (°C)	d(m)	$\frac{\bar{\rho}_2 - \bar{\rho}_1}{\bar{\rho}_1}$	$1.1\sqrt{gd\frac{\bar{\rho}_2 - \bar{\rho}_1}{\bar{\rho}_1}}$	$1.4\sqrt{gd\frac{\bar{\rho}_2 - \bar{\rho}_1}{\bar{\rho}_1}}$	Observed
CASE I	5	1220	1.97×10^{-2}	16.9	21.9	20.0
(ΔP=2.2mb)	4	1500	1.91×10^{-2}	18.6	23.6	"
CASE II	5	3150	2.00×10^{-2}	27.1	35.1	"
(ΔP=6.2mb)	4	3900	1.93×10^{-2}	29.8	38.5	"

Radiosonde ascents penetrating the cold outflow of thunderstorm conducted by Thunderstorm Project personnel usually revealed the upper thermal boundary below 1525 m (Byers and Braham, 1949). Farquahrson (1937) and Simpson (1969) have reported depths of intense haboobs in Sudan of 1100 to 1500 m. The depth values in CASE I indicate the 31 May 1969 outflow air mass was relatively deep. On the other hand, the depth values under CASE II exceed all previous thunderstorm-outflow depth estimates known to the author.

The density ratio, $(\bar{\rho}_2 - \bar{\rho}_1)/\rho_1$, comprised of symbols denoting layer-means of the gust-front air and the ambient air displaced by the gust front, is obtained as illustrated in figure 15. Since the density-versus-height curves in figure 15 are practically straight lines, the values of ρ_2 and $\bar{\rho}_1$ are assigned the densities at the mid-levels of the respective air layers. The density ratios are tabulated in table 3.

The substitution of these numerical values of the mean depths and density ratios into (6) and (7) gives the displacement speed of the gust-front air mass propagating as a gravity current. For CASE I, gratifying agreement to the observed speed[10] is obtained from both equations, especially for the 4°C temperature drop (considered to be a more realistic value). The larger theoretical speed given by von Karman's relation (second "displacement speed" column in table 3) is expected, because energy dissipation processes that retard horizontal motion in the actual flows are not taken into account. These computational results indicate that if the assumption about the upper temperature profile of the cold air is not grossly incorrect, the overall agreement between theory and observation indicates that the governing dynamics of the 31 May gust front was similar to that of a gravity current.

The exceedingly large value of the gravity current displacement speed computed for CASE II is due to the inherently large value of cold-air depth. (Recall that this depth value was computed assuming that the successive pressure rises associated with the windshift and gust surge were due to the influx of high density air comprising the gust front.) This result adds support to the hypothesis (already employed previously) that the depth of cold air comprising the gust front is defined by the second pressure rise only; this agrees with the picture implied by the analytical fields (figures 9 to 12). This reasoning adds further support to the conclusion arrived at previously that the forerunning windshift and pressure jump were not characteristic features of the gust front structure.

6.4 Comparison of Detailed Structure of Gravity Currents and Gust Front

In section 6.3 the gross density structure of the 31 May gust front was employed for examination of its horizontal propagation as a gravity current. Application of elementary gravity current theory demonstrated that its observed displacement did approximate that of a gravity current according to a model on which the theory is based. We have already alluded to an example of a laboratory gravity current (figure 16a) that exhibited a distinctive surface boundary shape. Such laboratory currents have further revealed a systematic internal circulation and mass entrainment pattern near the leading edge. In the following paragraphs, the detailed analytical structure of the gust front is examined for analogous features.

---

[10] The "observed speed" in table 1 is the gust front displacement relative to the flow of the lower tropospheric environment.

6.4.1 Geometric Shape

Laboratory gravity currents display a typical surface boundary geometry, as exhibited in figure 16a. The surface profile in a vertical plane normal to the gravity-current front reveals a projecting nose a short distance above the lagging current front at the bottom. In upper regions, the density interface slopes backward, crests, and then slopes downward to form an elevated head at the current front. In this figure, the head depth appears to be only slightly greater than the mean upstream value; however, heads studied by Keulegan (1958) had about twice the depth of the upstream current for density ratios (as previously defined) similar to the gust front. In addition, density interface upstream of the head has generally been found to display a near-constant height.

The vertical profile of the density surge of the gust front below 444 m combined with the underlying surface pressure pattern imply a protruding nose some distance above the tower summit. The density-surge line exhibited a forward slope near the ground as shown in figure 13; the average slope in the lowest 100 m is 65°.[11] This density-surge slope is maintained through the tower depth. But, if we assume the surface pressure at WKY directly below the density discontinuity is hydrostatic, the cold-air boundary above the tower top must begin a rearward slope within several hundred meters to be consistent with the surface pressure change. Thus, a protruding nose is envisioned similar to those seen in figure 17.

Simpson (1969) observed similar nose shapes in sea-breeze fronts. Note that the deduced gust-front nose, as well as the noses in the other examples referenced above, have a general shape similar to those leading laboratory gravity-current surges (figure 16a). However, in other studies, Koschmieder (1936, 1941) found that the heading cold-air profile changes in time and space in individual sea-breeze fronts, and Colmer (1971) observed that the leading horizontal wind-shear profile varied from one gust-front case to the other. This finding prompted them to suggest that the cold air comprising the projecting nose to periodically collapse, in a cyclic manner, into the warm air beneath it.

---

[11] The forward slope of the gust surge was 85°, significantly greater than that exhibited by the density-surge line, in agreement with the findings of Goldman and Sloss (1969). The probable reason for the greater slope of the gust-surge profile is the unlimited frictional retardation of the wind near the ground. On the other hand, the slope of the thermal profile is limited by overturning, which commences when the overlying cold air projects too far over the warm air.

In this regard, the narrow thermal ridge ahead of the density-surge line (figure 11c) and beneath the just-inferred nose may indicate subsiding air motion and the beginning stage of the nose collapse.[12] On the other hand, the stream function analysis does not reveal downward flow below the nose, i.e., in the area of figure 9d bounded by the time interval 2338 to 2339 CST and the layer 0 to 300 m. However, this apparent contradiction can be subjectively countered by considering that such a small-scale feature as a collapsing nose would probably not be resolved by such an analysis.

The surface pressure distribution and thermal structure of the overlying gust front, just upstream of the protruding nose, were used to infer an elevated crest of cold air. The pressure traces at WKY and 2C exhibit a pressure peak just upstream of the maximum wind cell (figures 10 and 13). This excess pressure maximum at WKY is shown as 2.5 mb in figure 13. In the region of the pressure maximum, the average surface-to-444 m temperature difference from the displaced warm air is only 3.5°C. Employing these parameter values to compute the depth of the cold air, according to the procedure described previously, yields 1700 m. This depth exceeds the uniform upstream level of 1220 m (CASE I, table 3) by 480m. Henceforth, this vertical bulge in cold-air height will be called "elevated head," in conformity with the term applied to an analogous feature in laboratory gravity currents. The horizontal distance between the head and the nose is 4 km; the uniform depth upstream begins 7.5 km from the nose. The mean dimensions of heads appearing in Keulegan's (1958) laboratory gravity currents, "blown-up" to the scale of the gust front, are head of height 2500 m, positioned 5 km upstream from the nose, while the upstream constant depth region begins at 7.5 km from the nose. This comparison shows that although the horizontal dimension is similar, the vertical dimension of the gust-front head is much suppressed compared with heads exhibited by gravity currents in stratified liquids in Keulegan's experiments.

A scan of meteorological literature for previous discoveries of elevated heads at the front of cold surges yielded several examples. From plots of the height of the vertical wind shear maximum (assumed to coincide with the frontal surface) with horizontal distance from the leading edge of four cold fronts in Australia, Berson (1958) found that most cases revealed a shallow "dip" in otherwise upsloping shear profiles. An example, reproduced from his article, is seen in figure 19. Berson called the small height maximum in the shear profile between the leading edge and the dip a "friction head" as an analogy to heads in laboratory gravity currents. The horizontal distance of the dip from the leading surface position of the shear zone was between 13 to 59 km, as the actual

[12] Observations of the wind and thermal structure at the leading edge of gust fronts, suggestive of all stages of this cyclic process, have been noted by the author in preliminary investigation's of other gust-front cases.

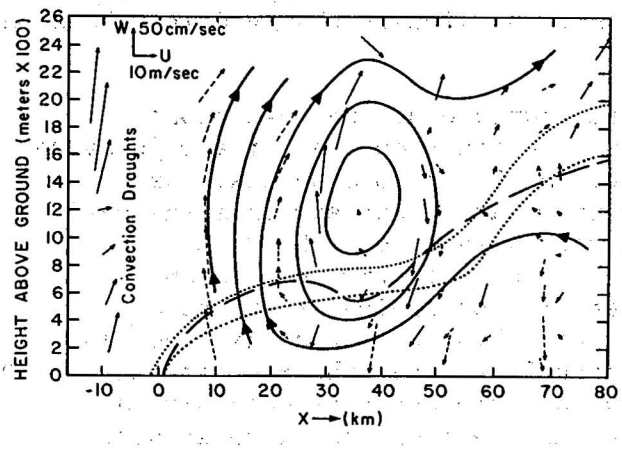

Figure 19. A composite analysis of the wind field near the leading edge of a cold front in Australia (after Berson, 1958). The dashed and dotted curves represent zones of maximum vertical wind shear. These shear zones are assumed to correspond approximately to the frontal surfaces. Note the dip or level region in the shear profiles in the vicinity of 40 km from the leading edge of the front. The flow pattern is shown relative to a coordinate axis translating to the left along with frontal boundary. The streamlines are drawn roughly to fit the plotted wind vectors.

location varied from front-to-front as well as in time and space in individual fronts. Clarke's (1961) vertical section analyses through cold fronts and sea-breeze fronts in Australia, in many cases, exhibited vertical bulges in the temperature and streamline fields near the leading edge, suggestive of frontal heads on a scale similar to those found by Berson (1958). In view that vertical and horizontal dimensions of laboratory gravity-current heads are not far different, Clarke would not submit that these bulges were the counterpart of heads seen in the laboratory. Instead, he reserved the possibility that heads of much smaller horizontal dimension may have existed in the fronts he examined, but, they could not be identified because of the insufficient density of his pibal and rawinsonde measurements. With the aid of Doppler wind measurements and rawinsondes, Browning and Harrold (1970) deduced a small frontal surface "nose" (identical to the head as defined in this paper) at the crest of an abrupt rise of the leading cold-air boundary to 1 km followed by a temporary upstream fall. The horizontal dimension was about 10 km. However, an attempt to interpret this head as an analogy to gravity-current heads requires that great caution be exercised.[13] In

[13] The scale of Browning and Harrold's (1970) analyses (as well as of the squall-line analyses performed by Newton, 1950) implies that the identification of a feature the size of the head would be quite difficult and, furthermore, an attempt to interpret such a feature is frustrated by likely complications introduced by the overhead intense convection currents associated with the heavy precipitation. On the other hand, a gust front, which is the low-level cold outflow from the convective precipitation, is a smaller scale atmospheric current, requiring a relatively small-scale analysis to identify a feature the size of the head such as that found in the case of the 31 May gust front. Since the head deduced in the latter analysis was 15 to 20 km downstream from the heavy precipitation its interpretation is less difficult.

conclusion, in view that the typical gust front is of a smaller scale than cold fronts, and since it usually exhibits a more intense initial surge, it is not surprising that the 31 May gust-front head had a larger vertical dimens: and smaller horizontal dimension than those previously observed in cold fronts and sea-breeze fronts.

The shape of the top of the cold-air surface of the gust front, upstream of the elevated head, was also inferred from the surface pressure pattern in the overlying cold air. Figures 10 and 13 show that the pressure at WKY and 2C was practically invariant upstream from the head region up to the position of the heavy rain area denoted by R in figure 10.[14] The thermal distribution is shown, in figures 11a and 11c, to be slowly decreasing in the coincident region upwind of the head. If we assume that the surface pressure over this horizontal distance is hydrostatic and bar compensating mass transfers above the gust front, these pressure and thermal fields imply that the depth of cold air was relatively uniform or perhaps decreasing upstream of the elevated head. For simplicity the cold-air depth in this region is assumed to have a constant value and equal to 1350 m, which is a rough average of CASE I in table 3 (see figure 21). Recall that the laboratory gravity currents also feature a uniform depth in the analogous span of the current.

The observation of uniform cold-air depth in the sector of cold surges, where frictional stress and horizontal pressure forces are in approximate balance, has some documented precedence. From a theoretical analysis, Ball (1960) has shown that when frictional stress is taken into account in the equations of motion, the solutions reveal that the slopes of frontal surfaces are grossly different than the frontal slope given by the Margules relation for the case of assumed geostrophic flow. In the former case, the frontal inversions tend to become horizontal with increasing distance from the cold front. Clarke (1961) showed that approximate frictional balance extends to about 30 km upstream of the leading edge of cold fronts and sea-breeze fronts in Australia. Farther upstream, geostrophic balance predominates. These findings (Ball, 1960; and Clarke, 1961) seem to be consistent with the shallow dips appearing in Berson's (1958) and Browning and Harrold's (1970) frontal analysis.

In view of Ball's and Clarke's results, it is likely that the air motion within the 31 May gust front was almost entirely governed by frictional stress and horizontal hydrostatic pressure gradient. Recall that the upper surface of the gust front was deduced to be horizontal or even downward-sloping with increasing distance from the leading edge. Furthermore, the observation of steady horizontal displacement (see p. 17) suggests the cold outflow current was in approximate balance between the frictional and the pressure gradient forces. Considering the extreme horizontal and vertical wind shears that existed at the boundaries of the air mass (see bottom of p. 22), it is not surprising that such large

[14] The surface pressure is known to rise sharply in the region where heavy rain is accompanied by intense cold downdrafts, as shown by Fujita (1963).

frictional stresses, as are necessary to balance the observed horizontal pressure gradient, apparently occurred inside the gust front.

Thus, it has been demonstrated that the observed and deduced shapes of the 31 May gust front's bounding surfaces exhibit a clear resemblance to the shape of experimental gravity currents. In addition, some gross deductions based on the results of Ball's (1960) and Clarke's (1961) studies indicated that the steady, horizontal air current comprising the gust front was governed by a balance of forces, identical to those acting in gravity flows. However, we have jet to consider the analytical three-dimensional circulation and gustiness patterns inside the gust front on the one hand, and identical features observed in gravity currents on the other.

6.4.2 Internal Circulation and Gustiness

Laboratory studies of gravity currents have revealed the environment flow relative to the forward motion of the head and the internal circulation fields in a vertical plane normal to the leading edge of such flows. Middleton's (1966) observations of the flow field relative to the motion of the elevated head resemble a pattern characteristic of flow around a solid body. This picture implies that when the head is translating horizontally at a rapid rate, upward motion of ambient fluid above the nose would be substantial. The internal flow of laboratory gravity currents features a strong forward horizontal current, an undercurrent, a short distance above the bottom. The speed of the undercurrent is greater than the forward speed of the head. Consequently, the flow is deflected upwards through the nose and then rearward near the crest of the head (see figure 20).

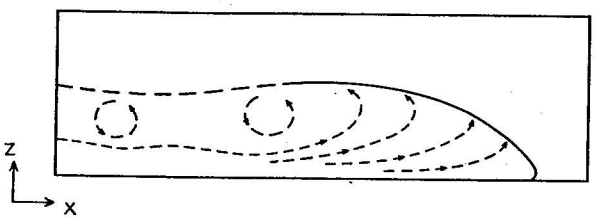

Figure 20. Internal circulation pattern of laboratory gravity currents as seen by a coordinate axis translating to the right with the speed of the head (after Middleton, 1966).

The analysis of the flow pattern of the gust front in a vertical plane features a strong ambient air flow towards the head of the gust front and large upward ambient-air motion near the nose, indicative of up-sliding flow over the head. This flow pattern is constructed by first considering that relative to a coordinate axis attached to the head, the environmental flow in the lowest 500 m is directed toward the head at approximately 20 m sec^{-1}. Now, the stream function field (figure 9d) discloses upward velocity ahead of the nose and as fast as 2.5 m sec^{-1} is maintained from just above the ground to the top level. A rough upper-bound estimate of the average vertical velocity of air parcels, being mechanically lifted by the head from the ground to 1700 m, is 4 m sec^{-1}. This estimate agrees with Doppler radar vertical velocity

measurements over an intense cold front accompanied by convective precipitation (Browning and Harrold, 1970).

The stream function analysis of the wind current normal to the density-surge line shows that cold air actually flowed across the density-surge zone. This is seen (figure 9d) by an initial consideration that there is no relative flow across the superposed 20 m sec^{-1} isotach since the assumed coordinate system is moving at the same speed. However, immediately to the left of this isotach, the streamline flow is forward and thus across the superposed density-surge line. This result is not without uncertainty, however, because of the short distance separating the 20 m sec^{-1} isotach and the density-surge line and accurate resolution the stream function field is questionable on such a small scale, particularly near the discontinuity zones.

The ambient air flow toward and over the cold outflow head and the cross-density-surge flow of the cold air are illustrated in figure 21. Although the streamlines are drawn schematically, their spacing qualitatively depicts the flow speed. The streamline flow at heights above the nose was drawn subjectively under the restrictions of conservation of mass and no flow across the cold-air boundary. The ambient-air streamline pattern near the head is seen to be quite similar

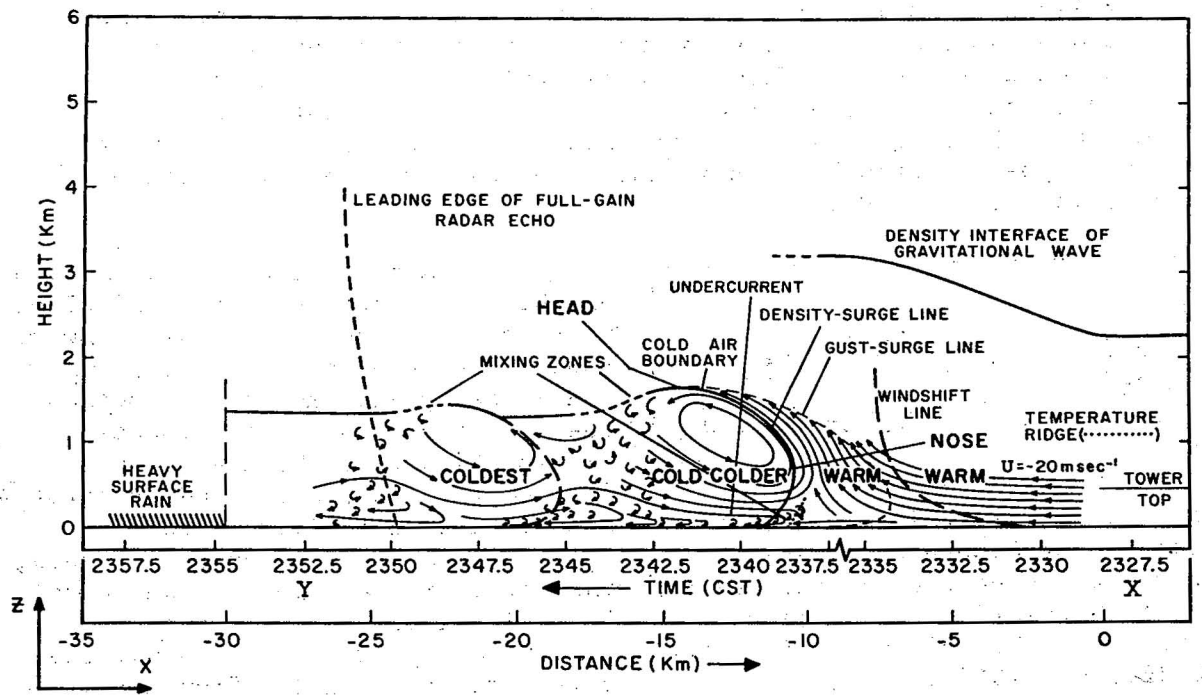

Figure 21. A composite schematic model combining the features of the analyzed and deduced structure of the windshift and gust front leading the squall line of 31 May 1966. (See the text for discussion.)

to that observed in laboratory experiments (Middleton, 1966; and Simpson 1969). It is also consistent with observations of dust being lifted to great heights at the leading edge of intense cold surges, as exemplified in figure 17. The cross-density-surge flow is in accord with analyses of cold fronts and sea-breeze fronts by Berson (1958) and Clarke (1961). (An example, taken from Berson's article, is shown in figure 19). Furthermore, it allows for dust to be picked up within the cold air (where winds are likely to be strongest, as in this case) and then to be transported horizontally to the region of maximum vertical velocity just ahead of the projecting cold-air nose; in this position, the dust could be transported upwards to the crest of the head as shown in figure 17.

The average speed of the cold-air current, upstream of the elevated head, was approximately the same as the horizontal displacement speed of the gust-front head. This mean current speed, representing the average of horizontal velocity components in the vertical plane upstream of the initial surge in figure 9d, was 21.5 m sec^{-1}. The displacement speed of the head was 21.0 m sec^{-1}. Applying Prandtl's (1952) expression for the horizontal propagation of an ideal cold front, yields the result that the cold air moves about one-half the speed of the mean upstream current. Thus his expression seriously underestimates the actual propagation speed of the gust front. Clarke (1961) obtained a similar result in his application of Prandtl's relation to sea-breeze flows and cold fronts in Australia.

A distinct vertical circulation field in a vertical plane normal to the leading edge of the gust front is deduced from the surface-to-444 m vertical section analyses (figure 9d and 9f). In the region of the head, a strong forward current of relative speed 13 m sec^{-1} is centered only 180 m above the ground (figure 9f). This jet-like current is henceforth termed undercurrent, as an analogy to a similar feature appearing in laboratory gravity currents. (It is interesting to add that Simpson's (1969) laboratory currents revealed a value of 1.3 for the ratio of the undercurrent speed to the propagation speed of the head. The analogous ratio for the gust front was 1.6.) The undercurrent was diverted upward in the region of the gust-front nose. Downward air flow occurred in the wake region of the head, in broad agreement with a similar feature appearing in the analysis of cold fronts and sea-breeze fronts by Berson (1958), Clarke (1961), and Browning and Harrold (1970). Figure 9d reveals downward motion at 400 m approaching 1 m sec^{-1}. Note that the zone of maximum downward speed in figure 9d coincides with a positive temperature anomaly of 2°C in figure 11c, implying subsidence of potentially warmer air. Downward air-parcel displacements of almost 200 m are indicated. These analytical features can be interpreted to mean that the cold-air flux that supplied the high-speed undercurrent came partly from air that had subsided from some height on the back of the head, and partly from the gradually subsiding current originating far upstream of the head. Considering the downward flow on the back and upward flow on the front of the head (discussed earlier), mass continuity requires rearward air flow near the head crest. The actual flow pattern

below 444 m, as well as that envisioned above, is illustrated in figure 21. The weak secondary surge beginning at 2345 CST is not considered to be an important feature of the gust front, as stated earlier.

The streamline flow pattern shown in figure 21 shows only a slight resemblance to that obtained by Berson (1958) for cold fronts (see figure 19). The reason for the difference in the patterns may reside in the difference in data resolution and intensity of the cold-air surges. There is a more striking correspondence to Prandtl's (1952, pp 369-370) flow model of a cold front.

Coupled with the internal flow pattern, the wind gustiness and thermal fields are used to infer a complex ambient-air entrainment mechanism. First, the broad gustiness maximum in figure 9h superimposed on figure 9f coincides with the wake region of the initial maximum wind speed cell. Recall from p. 8 that the gustiness included airstream eddies of horizontal wavelength up to 3 km. Tower temperature records in the segment coinciding with both the broad thermal maximum, and the gustiness maximum, revealed temperature oscillations with horizontal wavelengths similar to the wavelengths of wind gusts. The peak amplitude of these temperature oscillations was 0.4°C, implying vertical air parcel displacements in the eddies of almost 40 m. Since such large eddies were concentrated in the wake region of the head where the vertical flow is towards the ground, it is reasonable to infer that turbulent mixing of cold and ambient air occurred along a diffuse interface on the back of the head crest; thence, the eddies were continuously carried downward to heights below 444 m by the downward flow. A second gustiness maximum, smaller in size but of greater intensity than the one discussed above (figure 9h), was located beneath the projecting nose.[15] Recall that this region is characterized by extreme vertical wind shear and slightly superadiabatic temperature lapse rate. Thus, the large eddies in the shearing current were not suppressed in this air column. Furthermore, the implication of cold- and warm-air mixing is consistent with the analytical feature depicting cross-density-surge flow in this portion of the gust front.

The mixing zones and related regions of large eddies are schematically illustrated in figure 21, the latter by short, curled arrows. The entrainment of ambient air into the head implies the gradual dilution of the cold air; however, this dilution is apparently counteracted by the continous influx of cold air, as shown in figure 21 by the inflowing streamlines originating far upstream.

Laboratory gravity currents reveal an ambient fluid entrainment mechanism similar to that deduced for the gust front. Keulegan (1958) and Middleton (1966) observed that the fluid volume in the wake region of

[15] This gustiness maximum would be a great hazard to aircraft in landing and take-off patterns at airports.

the head is a mixture of environment and high density fluid. This eddy infested mixture gradually descends and is slowly entrained into the undercurrent. This turbulent region is shown in figure 16a.[16] Simpson (1969) examined the fine details of the mixing process in laboratory flows and observed that the upper boundary of the head consists of bulges that roll up as they are swept backward, resembling Kelvin-Helmholtz instability billows along a density interface with shear. Figure 16b illustrates that large entrainment of ambient fluid occurs as the billows break up. Simpson (1969) suggested that a similar process occurs in sea-breeze fronts, after examining flight records of glider plane penetrating of such air-mass currents. The analyses of atmospheric cold surges by Berson (1958), Clarke (1961), and Browning and Harrold (1970), all show evidence of air entrainment upstream of the frontal head. A haboob photograph appearing in Farquharson's (1937) article reveals that in the upper region of the head the dust cloud resembles photographs of laboratory gravity currents (Keulegan, 1958, figure 27). All of these examples of actual observations of turbulent entrainment are broadly consistent with the deduced entrainment mechanism of the gust front illustrated in figure 21.

6.4.3 Dynamic Similarity of Gust Front and Gravity Currents

Use has already been made of the equation

$$V = k \sqrt{gd \frac{\Delta\rho}{\rho_1}} \qquad (8)$$

which relates the displacement speed, V, to the depth, d, of a gravity current of fluid density, ρ_2, and the density ratio, $\Delta\rho/\rho_1$, i.e., $\rho_2 - \rho_1/\rho_1$, where ρ_1 is the ambient fluid density. As discussed previously, when (8) is applied to atmospheric gravity-current phenomena, layer-mean densities should be used. In (8), k is a nondimensional number that can be interpreted as a ratio of the inertia of the current to the buoyancy force. This ratio defines the internal Froude number. From laboratory studies, Keulegan (1958) found that when d is the mean depth of the gravity current, k has a constant value of 1.1 for Reynold numbers greater than 1000. Recall that von Karman's (1940) theoretical value was 1.414. When the depth of the elevated head from Keulegan's currents was substituted for d, the mean value of k was found to be 0.76. Similar Froude numbers were obtained by Middleton (1966) in another laboratory study and by Daly and Pracht (1968) in numerical simulation experiments.

---

[16] There is no evidence of mixing beneath the nose of laboratory gravity currents. This presumably is due to the nose projecting over the less dense ambient fluid being quite small; in many experiments the nose overlap was not detected. In the atmosphere the analogous overlap can be large because of the large frictional retardation of the flow near the ground.

While (8) has been applied previously to the mean gust-front structure (see p. 37), the object here is to establish the Froude number of the gust front and to compare it with experimental values. Dynamic similarity is then discussed, taking into account physical similarities and differences in the source mechanism of both the gust front and gravity currents, as produced in the laboratory.

The internal Froude number computed for the gust front is found to be slightly larger than documented values for gravity currents and, in turn, even larger when compared with large-scale atmospheric cold surges. For the mean cold-air depth of 1350 m and density ratio as shown in table 3, k is equal to 1.25. When the head depth is employed in (8), k is 1.08. These two k values averaged about 25% greater than those obtained in Keulegan's experiments. In other documented examples of cold surges, four cold fronts examined by Berson (1958) and four by Clarke (1961) revealed almost identical Froude number averages, i.e., 0.55 and 0.59, respectively, about 25% less than experimental gravity currents. Froude numbers obtained from Clarke's (1961) and Simpson's (1969) sea-breeze analysis are somewhat conflicting but still average 12% less than experimental values. On the other hand, in the case of two haboobs exhibiting a mean propagation speed of 12.5 m sec^{-1} and mean depth 1300 m, Simpson (1969) reported a k value of 0.79. Since the 31 May gust front had about the same depth but moved almost twice as fast as these haboobs, this suggests that the k value of thunderstorm cold-air outflows is proportional to the propagational speed of the air mass.

The larger Froude number obtained for the 31 May gust front is perhaps expected in view of the apparent difference in the mechanism of its evolution and maintenance when compared with laboratory gravity currents and other atmospheric examples exhibiting gravity-current similarities. Recall from section 3 that the gust front became severe during the evolution of the mature stage of the LEWP as the parent echo attained high intensity and a fast forward speed. These observations suggest that the gust front initially evolved as high horizontal-momentum air inside the cumulonimbus cloud was transported to the ground in massive cold-air downdrafts. Then this mass of cold air at the base of the downdraft, already charged with large horizontal momentum, spread outwards as a gravity current. By this means, the gust front could maintain greater horizontal momentum than that derived solely from a balance of the frictional drag and the hydrostatic horizontal pressure gradient. The excess horizontal momentum of the outflow would, in turn, make the Froude number larger. For an ideal laboratory gravity-current experiment, a constant pressure head is maintained at the source to provide the high density fluid with sufficient initial forward momentum to continuously maintain the depth of the advancing fluid mass. In such a case, momentum at the source does not effect the displacement speed of the advancing head. When we consider this aspect, the source mechanism of laboratory gravity currents seems to be more similar to that of cold fronts and sea-breeze fronts than to the analogous mechanism of the gust front.

It is difficult to estimate that vertical transfer of horizontal momentum in the thunderstorm downdraft has on the momentum of the cold outflow of thunderstorms. Adding to the uncertainty is the unknown relationship between the horizontal speed of a cumulonimbus radar echo and the horizontal speed of air inside its downdraft. It is comparatively clear that the horizontal momentum of the downdraft could be a significant factor only when it is substantially greater than the horizontal momentum of the outflow due only to the influence of gravity.[17] This situation is likely in the formative stage of the gust front when the cold outflow is relatively shallow;[18] in such a case the gust front lies near the downdraft, and the streamline flow depicts a pattern envisoned when a jet of fluid strikes a plane surface at a small angle. The flow speed decreases sharply with normal distance from the jet core. However, once the amassed cold air becomes sufficiently deep and/or the horizontal momentum of the downdraft becomes sufficiently small, the cold outflow air evidently propagates approximately as a gravity current under relatively little influence of the downdraft momentum.

At the time of analysis of the 31 May gust front, the parent echo had already diminished somewhat in intensity, and the density surge had moved outward to a position 20 km ahead of the forward echo boundary. At the same time, the density surge was propagating 3 m sec^{-1} faster than the echo boundary. If we assume that the horizontal air speed within the downdrafts supplying the gust front was not far greater than the speed of the echo boundary, the effect on the propagational speed of the gust front head was probably minimal.

Thus, it is concluded that the predominant motive force for the gust-front propagation was gravity. The higher wind speeds over the northern part of the NSSL observation network (figure 9e) were due primarily to the larger horizontal pressure gradient in that region, apparently reflecting a greater depth of dense air.

In summary, approximate dynamic similarity between the 31 May gust front and gravity currents has been deduced. While the likelihood is small that high horizontal momentum injected into the outflow by the thunderstorm downdrafts was responsible for the slightly excessive Froude number, the possibility cannot be ruled out and remains a problem. The fundamental role of the downdraft as a source for the outflow was shown to be similar to the source mechanism used in experimental gravity current studies. However, the precise role of the downdraft in the formation and maintenance of thunderstorm gust fronts is still problematic.

---

[17] Actually, one can reason that the horizontal momentum of air at the base of the downdraft, greater than the momentum of the gust-front head, is required for the maintenance of the latter, because the outflow air mass is expected to lose momentum continuously due to friction in the region of near-zero pressure gradient between the head and the downdraft.

[18] Recall from (7) that the speed of a steady-state gravity current is directly proportional to the square root of its depth.

7. SUMMARY

A severe gust front leading the squall line of 31 May 1969 was analyzed to determine its three-dimensional structure and to investigate the mechanics of its horizontal propagation. All data measurements obtained by NSSL were used in the analysis.

The entire analysis of the leading part of the squall line was combined into a composite schematic model (figure 21). The initial change line, which preceded the leading edge of the cold outflow by 8 km, was a coincident windshift and pressure-jump line. The lack of data definition above 445 m, during the passage of this discontinuity, prevented a complete analysis. No evidence could be found to indicate that the windshift and pressure jump were due to cold-air advection associated with the gust front. Instead, substantial evidence indicates the discontinuity was due to a gravitational wave "jump" (Tepper, 1950, 1955) propagating on a 740-mb thermal inversion (figure 21). However, an attempt to determine a link between such a gravity wave and the gust front is beyond the scope of this analysis.

During the period of the analysis, the leading edge of the gust front was well ahead of the precipitation area (20 km ahead) and was propagating steadily at 21 m sec^{-1}. The radar echo from which the outflow emanated was in the "late" mature stage and was moving 3 m sec^{-1} slower than the gust front.

The shape of the cold-air outflow constituting the gust front was defined in a vertical plane section taken normal to the line tangent to the leading edge. At the front of the cold air mass, a "projecting nose" was found, whose foremost extension was located about 750 m above ground level and 1.3 km forward of the cold-air boundary at the ground. The depth of the cold air exhibited a maximum of 1700 m near the front of the outflow air mass and immediately decreased to a near-uniform upstream value of about 1350 m (figure 21). Thus, an "elevated head" was located at the front of the air mass. The geometry of the air-mass profile is quite similar to the characteristic profile of the steady-flow gravity currents formed in stratified liquids in laboratory tank experiments (Keulegan, 1958). It also agrees with the shape of cold "kata-fronts" (Ball, 1960) where frictional stress is taken into account in the equations of motion.

The ambient air flow toward the head, which is deflected upwards in the nose region, and the circulation field inside the cold air mass is also similar to analogous flow features revealed by laboratory gravity currents. Just ahead of the nose, upward velocities up to 2.5 m sec^{-1} at the 400 m level were computed, and values up to 5 m sec^{-1} at higher levels were inferred as the ambient air flow was lifted up and over the head (as seen by a coordinate axis translating with the head at 20 m sec^{-1}). Inside the head, the circulation field featured a horizontal wind speed maximum of 13 m sec^{-1} (with respect to the trans-

lating reference axis) at a height of only 180 m above the ground (figure 21). This feature may correspond to the "undercurrent" in laboratory gravity flows. This undercurrent is deflected upwards in the nose region and finally rearward near the crest of the head. In the wake region of the head, where general downward air motion is evidenced by analyzed downward components up to 1 m sec^{-1} at 400 m, the wind velocity and temperature fields were quite turbulent. Eddy mixing of ambient air in the wake of the head crest and a steady downward flux of this air mixture is postulated to explain these observations. Vigorous eddy mixing is also implied beneath the nose. These entrainment mechanisms evidently tended to erode the cold-air head, but this erosion was counteracted by inflow of cold air from the upstream direction. This ambient and internal flow field associated with the gust front is remarkably similar to analogous features of gravity currents as deduced by Prandtl (1952) and observed in laboratory experiments (Middleton, 1966; Simpson, 1969).

The similarity of internal Froude numbers of the gust front and laboratory gravity currents indicates mutual dynamical similarity. The gust front Froude number was only 25% larger than those associated with laboratory currents; however, the percentage excess is greater when comparing with larger scale atmospheric cold surges. It is reasoned that Froude numbers of thunderstorm outflow air masses are sometimes larger than those revealed by other atmospheric cold surges because the horizontal displacement speed of the outflow may be boosted by the injection of high horizontal-momentum air, perhaps originating from a mid-tropospheric level. However, during the period of analysis of the 31 May case such an influence was likely to be small (as the near correspondence of Froude numbers would suggest because the gust front was propagating faster than the parent echo while the latter was in the later mature stage.

8. ACKNOWLEDGEMENTS

The author extends sincere appreciation to Professor Yoshikazu Sasaki who, as supervisor of my research, rendered timely personal encouragement and technical guidance. This counseling was a major contribution towards the completion of this study.

The author is also deeply indebted to all the NSSL personnel who assisted in gathering the data used in this research. Special thanks are due to NSSL staff, who provided data and special equipment for aiding in its analyses. Mr. J. T. Dooley's promptness in assembling the data package and his assistance in the data interpretation also bears special thansk. Drs. Stan Barnes (NSSL) and Rex Inman (O. U.) and Gene Wilkins (O. U.) and Messrs. Ken Wilk and Dale Sanders contributed many helpful suggestions and criticisms during the course of the research and subsequently, on the original manuscript.

It is a pleasure to acknowledge with thanks the contribution of fellow students and staff of the O. U. Department of Meteorology. Don Holyoke, Bill Parton, Bob Sheets and Keven Amerin deserve special mention. Carlos Droescher performed the drafting.

9. REFERENCES

Ball, F. K. (1960), A theory of fronts in relation to surface stress. Quart. J. Roy. Meteor. Soc., 86, 51-66.

Barclay, P. A. and K. E, Wilk (1970), Severe thunderstorm radar echo motion and related weather events hazardous to aviation operations. National Severe Storms Laboratory, Tech. Memo. ERLTM-NSSL 46, 63 pp.

Benjamin, T. B. (1968), Gravity currents and related phenomena. Part 2, J. Fluid Mech, 31, 209-248.

Berson, F. A. (1958), Some measurements of undercutting cold air. Quart. J. Roy. Meteor. Soc., 84, 1-16.

Browning, K. A. and T. W. Harrold (1970), Air motion and precipitation growth at a cold front. Quart J. Roy. Meteor. Soc., 96, 369-389.

Byers, H. R. and R. R. Braham, Jr. (1949), The Thunderstorm. Washington, D. C., U. S. Government Printing Office, 287 pp.

Carter, J. K. (1970), The meteorological instrumented WKY-TV tower facility. National Severe Storms Laboratory, Tech. Memo. ERLTM-NSSL 50, 18 pp.

Charba, J. and Y. Sasaki (1971), Structure and movement of the severe thunderstorms of 3 April 1964 as revealed from radar and surface mesonetwork data analysis. J. Meteor. Soc. Japan, 49, 191-214.

Clarke, R. H. (1961), Mesostructure of dry cold fronts over featureless terrain. J. Meteor., 18, 715-735.

Colmer, M. J. (1971), On the characteristics of thunderstorm gust fronts. Roy Aircraft Est., Bedford, Eng. 11 pp.

Cook, B. J. (1961), Some LEWP observations and associated severe weather. Proc. Ninth Wea. Radar Conf. Am. Meteor. Soc., Boston, Mass., pp. 181-185.

Daly, B. J. and W. E. Pracht (1968), Numerical study of density-current surges. Phys. Fluids, 10, 15-30.

Farquharson, J. S. (1937), Haboobs and instability in Sudan. Quart. J. Roy. Meteor. Soc. 63, 393-414.

Fujita, T. (1959), Precipitation and cold-air production in mesoscale thunderstorm systems. J. Meteor., 16, 454-466.

Fujita, T. (1963), Analytical mesometeorology: a review. Meteor. Monogr., 5, 77-125.

_____, (1966), Detailed investigation of mesometeorological conditions of the squall line of August 6-7, 1966 which crossed the air route between Kansas City, Missouri and Omaha, Nebraska. Part III: Turbulence in relation to the squall line. Prepared for the British Aircraft Corp., Inc., USA, 27 pp.

Goldman, J. L. and P. W. Sloss (1969), Structure of the leading edge of thunderstorm cold-air outflow. Proc. Sixth Conf. on Severe Local Storms, Am. Meteor. Soc., Boston, Mass., pp 71-79. (unpublished manuscript.)

Koschmieder, H. (1936), Danziger Seewind Studien I. Forch Met. Inst., Danzig, 8, 49 pp.

_____, (1941), Danziger Seewind Studien II, Ibid., 10, 39 pp.

Keulegan, G. H. (1958), Twelfth progress report on model laws for density currents; the motion of saline fronts in still water. U. S. Natl. Bur. Standards, Rept. No. 5831, 28 pp.

Lamb, H. (1932), Hydrodynamics. Cambridge University Press, 280.

Lidga, M.G.H. and S. G. Bigler (1958), Radar echoes from a cloudless cold front. J. Meteor., 15, 494-501.

Middleton, G. V. (1966), Experiments on density and turbidity currents. I. Motion of the head. Can. J. Earth Sci., 3, 523-546.

Nolen, R. H. (1959), A radar pattern associated with tornadoes. Bull. Am. Meteor. Soc., 40, 277-279.

Newton, C. W. (1950), Structure and mechanism of prefrontal squall line. J. Meteor, 7, 210-222.

Prandtl, L. (1952), Essentials of Fluid Dynamics. London, Blackie and Son., 452 pp.

Sasaki, Y. (1970), Numerical variational analysis with weak constraint and application to surface analysis of severe storm gust. Mon. Wea. Rev., 98, 399-410.

Simpson, J. E. (1969), A comparison between laboratory and atmospheric density currents. Quart. J. Roy. Meteor. Soc., 95, 758-756.

Tepper, M. (1950), A proposed mechanism of squall lines: The pressure jump line. J. Meteor., 7, 21-29.

_____, (1955), On the generation of pressure jump lines by the impulsive addition of momentum to simple current systems. J. Meteor., 12, 287-297.

von Karman, T. (1940), The engineer grapples with nonlinear problems. Bull. Am. Math. Soc., 46, 615-683.

Yih, C.-S. (1969), Stratified flows. The Annual Review of Fluid Mechanics Palo Alto, Calif. Annual Rev., Inc., pp. 106-108.

NATIONAL SEVERE STORMS LABORATORY

The NSSL Technical Memoranda, beginning with No. 28, continue the sequence established by the U. S. Weather Bureau National Severe Storms Project, Kansas City, Missouri. Numbers 1-22 were designated NSSP Reports. Numbers 23-27 were NSSL Reports, and 24-27 appeared as subseries of Weather Bureau Technical Notes. These reports are available from the National Technical Information Service, Operations Division, Springfield, Virginia 22151, for $3.00, and a microfiche version for $0.95. NTIS numbers are given below in parentheses.

No. 1 National Severe Storms Project Objectives and Basic Design. Staff, NSSP. March 1961. (PB-168207)

No. 2 The Development of Aircraft Investigations of Squall Lines from 1956-1960. B. B. Goddard. (PB-168208)

No. 3 Instability Lines and Their Environments as Shown by Aircraft Soundings and Quasi-Horizontal Traverses. D. T. Williams. February 1962. (PB-168209)

No. 4 On the Mechanics of the Tornado. J. R. Fulks. February 1962. (PB-168210)

No. 5 A Summary of Field Operations and Data Collection by the National Severe Storms Project in Spring 1961. J. T. Lee. March 1962. (PB-165095)

No. 6 Index to the NSSP Surface Network. T. Fujita. April 1962. (PB-168212)

No. 7 The Vertical Structure of Three Dry Lines as Revealed by Aircraft Traverses. E. L. McGuire. April 1962. (PB-168213)

No. 8 Radar Observations of a Tornado Thunderstorm in Vertical Section. Ralph J. Donaldson, Jr. April 1962. (PB-174859)

No. 9 Dynamics of Severe Convective Storms. Chester W. Newton. July 1962. (PB-163319)

No. 10 Some Measured Characteristics of Severe Storms Turbulence. Roy Steiner and Richard H. Rhyne. July 1962. (N62-16401)

No. 11 A Study of the Kinematic Properties of Certain Small-Scale Systems. D. T. Williams. October 1962. (PB-168216)

No. 12 Analysis of the Severe Weather Factor in Automatic Control of Air Route Traffic. W. Boynton Beckwith. December 1962. (PB-168217)

No. 13 500-Kc./Sec. Sferics Studies in Severe Storms. Douglas A. Kohl and John E. Miller. April 1963. (PB-168218)

No. 14 Field Operations of the National Severe Storms Project in Spring 1962. L. D. Sanders. May 1963. (PB-168219)

No. 15 Penetrations of Thunderstorms by an Aircraft Flying at Supersonic Speeds. G. P. Roys. Radar Photographs and Gust Loads in Three Storms of 1961 Rough Rider. Paul W. J. Schumacher. May 1963. (PB-168220)

No. 16 Analysis of Selected Aircraft Data from NSSP Operations, 1962. T. Fujita. May 1963. (PB-168221)

No. 17 Analysis of Methods for Small-Scale Surface Network Data. D. T. Williams. August 1963. (PB-168222)

No. 18 The Thunderstorm Wake of May 4, 1961. D. T. Williams. August 1963. (PB-168223)

No. 19 Measurements by Aircraft of Condensed Water in Great Plains Thunderstorms. George P. Roys and Edwin Kessler. July 1966. (PB-173048)

No. 20 Field Operations of the National Severe Storms Project in Spring 1963. J. T. Lee, L. D. Sanders and D. T. Williams. January 1964. (PB-168224)

No. 21 On the Motion and Predictability of Convective Systems as Related to the Upper Winds in a Case of Small Turning of Wind with Height. James C. Fankhauser. January 1964. (PB168225)

No. 22 Movement and Development Patterns of Convective Storms and Forecasting the Probability of Storm Passage at a Given Location. Chester W. Newton and James C. Fankhauser. January 1964. (PB-168226)

No. 23 Purposes and Programs of the National Severe Storms Laboratory, Norman, Oklahoma. Edwin Kessler. December 1964. (PB-166675)

No. 24 Papers on Weather Radar, Atmospheric Turbulence, Sferics, and Data Processing. August 1965. (AD-621586)

No. 25 A Comparison of Kinematically Computed Precipitation with Observed Convective Rainfall. James C. Fankhauser. September 1965. (PB-168445).

No. 26 Probing Air Motion by Doppler Analysis of Radar Clear Air Returns. Roger M. Lhermitte. May 1966. (PB-170636)

No. 27 Statistical Properties of Radar Echo Patterns and the Radar Echo Process. Larry Armijo. May 1966. The Role of the Kutta-Joukowski Force in Cloud Systems with Circulation. J. L. Goldman. May 1966. (PB-170756)

No. 28 Movement and Predictablity of Radar Echoes. James Warren Wilson. November 1966. (PB-173972)

No. 29 Notes on Thunderstorm Motions, Heights, and Circulations. T. W. Harrold, W. T. Roach, and Kenneth E. Wilk. November 1966. (AD-644899)

No. 30 Turbulence in Clear Air Near Thunderstorms. Anne Burns, Terence W. Harrold, Jack Burnham, and Clifford S. Spavins. December 1966. (PB-173992)

No. 31 Study of a Left-Moving Thunderstorm of 23 April 1964. George R. Hammond. April 1967. (PB-174681)

No. 32 Thunderstorm Circulations and Turbulence from Aircraft and Radar Data. James C. Fankhauser and J. T. Lee. April 1967. (PB-174860)

No. 33 On the Continuity of Water Substance. Edwin Kessler. April 1967. (PB-175840)

No. 34 Note on the Probing Balloon Motion by Doppler Radar. Roger M. Lhermitte. July 1967. (PB-175930)

No. 35 A Theory for the Determination of Wind and Precipitation Velocities with Doppler Radars. Larry Armijo. August 1967. (PB-176376)

No. 36 A Preliminary Evaluation of the F-100 Rough Rider Turbulence Measurement System. U. O. Lappe. October 1967. (PB-177037)

No. 37 Preliminary Quantitative Analysis of Airborne Weather Radar. Lester P. Merritt. December 1967. (PB-177188)

No. 38 On the Source of Thunderstorm Rotation. Stanley L. Barnes. March 1968. (PB-178990)

No. 39 Thunderstorm - Environment Interactions Revealed by Chaff Trajectories in the Mid-Troposphere. James C. Fankhauser. June 1968. (PB-179659)

No. 40 Objective Detection and Correction of Errors in Radiosonde Data. Rex L. Inman. June 1968. (PB-180284)

No. 41 Structure and Movement of the Severe Thunderstorms of 3 April 1964 as Revealed from Radar and Surface Mesonetwork Data Analysis. Jess Charba and Yoshikazu Sasaki. October 1968. (PB-183310)

No. 42 A Rainfall Rate Sensor. Brian E. Morgan. November 1968. (PB-183979)

No. 43 Detection and Presentation of Severe Thunderstorms by Airborne and Ground-Based Radars: A Comparative Study. Kenneth E. Wilk, John K. Carter, and J. T. Dooley. February 1969. (PB-183572)

No. 44 A Study of a Severe Local Storm of 16 April 1967. George Thomas Haglund. May 1969. (PB-184-970)

No.45 On the Relationship Between Horizontal Moisture Convergence and Convective Cloud Formation. Horace R. Hudson. March 1970. (PB-191720)

No. 46 Severe Thunderstorm Radar Echo Motion and Related Weather Events Hazardous to Aviation Operations. Peter A. Barclay and Kenneth E. Wilk. June 1970. (PB-192498)

No. 47 Evaluation of Roughness Lengths at the NSSL-WKY Meteorological Tower. Leslie D. Sanders and Allen H. Weber. August 1970. (PB-194587)

No. 48 Behavior of Winds in the Lowest 1500 ft in Central Oklahoma: June 1966 - May 1967. Kenneth C. Crawford and Horace R. Hudson. August 1970.

No. 49 Tornado Incidence Maps. Arnold Court. August 1970. (COM-71-00019)

No. 50 The Meteorologically Instrumented WKY-TV Tower Facility. John K. Carter. September 1970. (COM-71-00108)

No. 51 Papers on Operational Objective Analysis Schemes at the National Severe Storms Forecast Center. Rex L. Inman. November 1970. (COM-71-00136)

No.52 The Exploration of Certain Features of Tornado Dynamics Using a Laboratory Model. Neil B. Ward. November 1970. (COM-71-00139)

No.53 Rawinsonde Observation and Processing Techniques at the National Severe Storms Laboratory. Stanley L. Barnes, James H. Henderson and Robert J. Ketchum. April 1971.

No. 54 Model of Precipitation and Vertical Air Currents. Edwin Kessler and William C. Bumgarner. June 1971.

No. 55 The NSSL Surface Network and Observations of Hazardous Wind Gusts. Operations Staff. June 1971.

No. 56 Pilot Chaff Project at the National Severe Storms Laboratory. Edward A. Jessup. November 1971.

No. 57 Numerical Simulation of Convective Vortices. Robert P. Davies-Jones and Glenn T. Vickers. November 1971.

No. 58 The Thermal Structure of the Lowest Half Kilometer in Central Oklahoma: December 9, 1966 - May 31, 1967. R. Craig Goff and Horace R. Hudson. July 1972.

No. 59 Cloud-to-Ground Lightning Versus Radar Reflectivity in Oklahoma Thunderstorms. Gilbert D. Kinzer. September 1972.

No. 60 Real Time Displays of Velocity Fields by Doppler Radar. L. D. Hennington and G. B. Walker. November 1972.